

Correspondence principle for many-body scars in ultracold Rydberg atoms

C. J. Turner, J.-Y. Desautels, K. Bull, and Z. Papić

School of Physics and Astronomy, University of Leeds, Leeds LS2 9JT, United Kingdom

(Dated: 28th May 2022)

The theory of quantum scarring – a remarkable violation of quantum unique ergodicity – rests on two complementary pillars: the existence of unstable classical periodic orbits and the so-called *quasimodes*, i.e., the non-ergodic states that strongly overlap with a small number of the system’s eigenstates. Recently, interest in quantum scars has been revived in a many-body setting of Rydberg atom chains. While previous theoretical works have identified periodic orbits for such systems using time-dependent variational principle (TDVP), the link between periodic orbits and quasimodes has been missing. Here we provide a conceptually simple analytic construction of quasimodes for the non-integrable Rydberg atom model, and prove that they arise from a “requantisation” of previously established periodic orbits when quantum fluctuations are restored to all orders. Our results shed light on the TDVP classical system simultaneously playing the role of both the mean-field approximation *and* the system’s classical limit, thus allowing to establish a rigorous link between the wavefunction scarring in the Rydberg atom chains and the single-particle quantum systems.

I. Introduction

Quantum scars provide a surprising connection between single-particle quantum billiards and their classical counterpart.^{1,2} The understanding of quantum scars is built upon the existence of unstable classical periodic orbits and atypical eigenstates. The former was first observed by studying the spreading of wave packets initialised along such orbits^{1,3} (see also Ref. 4). In the limit $\hbar \rightarrow 0$, the classical orbits are recovered, as stipulated by the correspondence principle.⁵ Furthermore, some atypical “scarred” eigenstates were found to concentrate around such orbits, in contrast to typical eigenstates at a similar energy, which tend to be well-spread across the whole configuration space. In the fully quantum case, the proof for the existence of scarred eigenstates relied on *approximate* eigenstates or “quasimodes”, which are constructed to be strongly localised around a classical periodic orbit. For example, in the celebrated Bunimovich stadium problem, quasimodes have the form $\psi(x, y) = \phi(x) \sin(n\pi y)$, i.e., they represent a standing wave in one direction with a suitably chosen envelope function in the other direction.^{2,6} By carefully controlling the density of states, it was possible to show that there exist eigenstates with an anomalously high overlap with a small number of quasimodes, hence “inheriting” their atypical properties.^{6–8}

Recently, similar non-thermal states have been identified in interacting quantum systems. These states, named quantum many-body scars by analogy, have been linked to long-lived oscillations measured in an experiment on a chain of Rydberg atoms.^{9–16} Since then, an increasing variety of models have been associated with various aspects of many-body scarring.^{17–48} In this work we focus on the “PXP” model – an idealised effective model of the Rydberg atom experiment^{49,50} – which can be formally expressed in terms of interacting spin-1/2 degrees of freedom, without an “obvious” semiclassical limit. Inspired by the theory of single-particle scars, an immediate question arises: what are the periodic orbits

and quasimodes in the PXP model?

Unlike single-particle billiards, the equivalent of the classical trajectory in the many-body case is less transparent. One proposal makes use of the Time-Dependent Variational Principle (TDVP),⁵¹ wherein many-body dynamics is projected onto a restricted manifold of matrix product states.^{52–54} Its application to the PXP model successfully captures the revivals following quenches from specific product states.^{11,24} It is thus natural to suggest that this approach defines an effective “semiclassical” description of the quantum dynamics, and holds the same relation with the exact PXP model as expected from the correspondence principle.

On the other hand, a family of quasimodes for the PXP model have also been independently constructed by the so-called Forward Scattering Approximation (FSA).^{10,55} This method makes it possible to extract properties of scarred eigenstates in systems much larger than those accessible by exact diagonalisation (ED). However, this way of building quasimodes presents some deficiencies, both on technical and conceptual levels. Indeed, while the computational cost of generating the FSA states is better than the exponential growth of the Hilbert space, it is still polynomial in the system size. Furthermore, the link between the FSA and the TDVP is obscure, thus making it difficult to relate the quasimodes with the classical limit of the model, in a manner that had been achieved for single-particle scars.

In this paper we introduce a new way to form quasimodes which resolves the aforementioned problems. Our construction relies on building a subspace symmetrised over permutations within each of the sublattices comprising even and odd sites in a chain. This approach can be thought of as a “mean-field” approximation, and makes it possible to obtain closed-form expressions for the projections of states and operators in this symmetric subspace. This enables us to numerically approximate highly-excited eigenstates of chains of length $N \lesssim 800$, far beyond other methods. Further, we show that the path-integral quantisation of the TDVP

topological space with a proper resolution of the identity *exactly* reproduces the symmetric subspace in the thermodynamic limit. While adding quantum fluctuations to the TDVP has been approximated to first order,⁵⁶ our method includes quantum fluctuations to *all* orders. This correspondence highlights the intriguing fact that TDVP in the PXP model serves as both a mean-field approximation and a classical limit taken together. We also show that the scarred quasimodes are localised around the TDVP periodic orbit, in a way that is reminiscent of single-particle quantum scars. Finally, performing time evolution in the symmetric subspace strongly suggests that the classical periodic orbit found in TDVP is stable to the addition of quantum fluctuations in the thermodynamic limit, at least to the “mean-field” level as described above.

II. Rydberg blockade and quantum scars

The PXP model is an effective model of a chain of atoms in the Rydberg blockade.⁴⁹ Denoting by $|\circ\rangle$ and $|\bullet\rangle$ the ground and excited states of each atom, the Hamiltonian is

$$H = \sum_{n=1}^N P_{n-1} X_n P_{n+1}, \quad (1)$$

where $X_n = |\circ\rangle\langle\bullet| + |\bullet\rangle\langle\circ|$ is the Pauli X and $P_n = |\circ\rangle\langle\circ|$ is a local projector. Here N denotes the number of sites in the chain and, unless specified otherwise, we assume periodic boundary conditions (PBCs), $N + 1 \equiv 1$. The projectors make the model in Eq. (1) constrained: a site can be excited only if both adjacent sites are in the ground state, e.g., the transition $|\dots\circ\circ\bullet\dots\rangle \rightarrow |\dots\circ\bullet\bullet\dots\rangle$ is forbidden. This causes a fracturing of the Hilbert space, which has a strong impact on its dynamical properties.^{57–62} Below we focus on the largest connected sector of the Hilbert space which contains no state with adjacent excitations.

The PXP model in Eq. (1) is non-integrable and thermalising,¹⁰ but it exhibits periodic revivals when quenched from certain initial states such as the Néel state, $|\mathbb{Z}_2\rangle = |\bullet\circ\bullet\circ\dots\rangle$. The observed revivals in the density of domain walls⁹ are remarkable given that the $|\mathbb{Z}_2\rangle$ state effectively forms an “infinite-temperature” ensemble for this system, for which the “strong” Eigenstate Thermalisation Hypothesis (ETH) predicts fast equilibration.^{63–66} Unlike many-body localised^{67–69} and integrable systems⁷⁰ which strongly break ergodicity, the PXP model breaks it only weakly.^{71,72} The breaking of ergodicity in the PXP model occurs most prominently due to the existence of a band of $O(N)$ scarred eigenstates, which have equal energy separation, anomalously high overlap with $|\mathbb{Z}_2\rangle$ state, and lowest entanglement among all eigenstates.⁵⁵ These states are the representatives of scarred towers of eigenstates (as can be seen in Fig. 2(a) below), which contain additional atypical eigenstates that exhibit clustering around the same energies and whose finite-size scaling

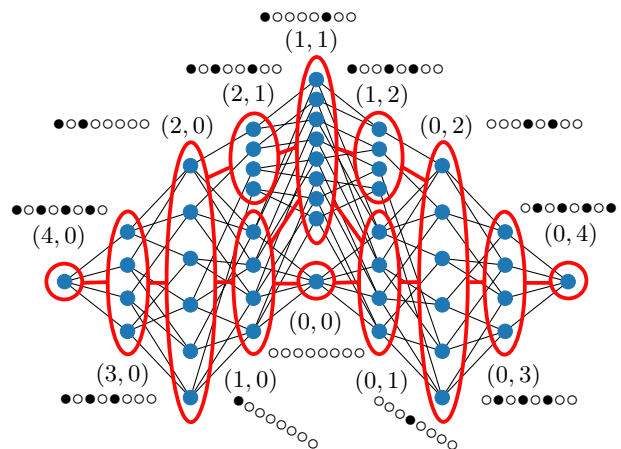


Figure 1. An example of the constrained Hilbert space of the PXP model in Eq. (1) for $N = 8$. Each blue dot represents an allowed product state of atoms compatible with the Rydberg constraint. The states are grouped into the equivalence classes of the symmetric subspace \mathcal{K} , denoted by ellipses. Each class is labelled by a representative state, e.g., the class $(0, 3)$ contains the representative state $\circ\bullet\circ\bullet\circ\bullet\circ\circ$ and all other obtained by permuting sites in each of the sublattices.

of inverse participation ratio is different from that of the thermalising eigenstates.¹⁰ The scarring properties in all of these special eigenstates are explained by the existence of quasimodes: simpler states with an underlying structure – the analogues of “standing waves” in billiard systems – which represent concentration points of the special eigenstates.

III. Construction of quasimodes

We construct quasimodes for the PXP model by first defining a symmetric subspace \mathcal{K} from a set of equivalence classes (n_1, n_2) , where integers n_1, n_2 label the number of excitations on the two sublattices, encompassing the odd and even sites, respectively. Elements in these classes are equivalent under the action of the product of two symmetric groups which “shuffle” the sites in each sublattice. This approach is somewhat reminiscent of the fully symmetric subspaces in the context of quantum de Finetti theorem⁷³ and in studies of fully-connected models.^{74,75} However, the key difference here is that the permutation symmetry is broken to the sublattice level, and many of the permutation shuffles violate the Rydberg constraint and therefore have to be excluded, which makes the analysis non-trivial. An illustration of the construction of \mathcal{K} for a PXP model of size $N=8$ is presented in Fig. 1.

We define an orthonormal basis for \mathcal{K} from the symmetric combinations of members of each class (n_1, n_2) ,

$$|(n_1, n_2)\rangle = \frac{1}{\#(n_1, n_2)} \sum_{x \in (n_1, n_2)} |x\rangle, \quad (2)$$

where $\#(n_1, n_2)$ is the size of the equivalence class.

The class sizes can be calculated analytically because the configurations can be generated by a recursive procedure or transfer-matrix problem which ‘glues’ sites (in the basis) onto the boundary of a smaller version of the same counting problem. Because the constraint on gluing an additional \bullet site is only sensitive to the state of the site immediately on the boundary, we can erase the information about the configurations further away and represent them by a count of all those configurations which are equivalent on the boundary. This produces a method for calculating $\#(n_1, n_2)$ using dynamic programming in only polynomial time. It can be shown⁷⁶ that the class sizes admit the closed-form expression

$$\#(n_1, n_2) = \frac{N}{2} \binom{\frac{N}{2} - n_1 - n_2}{\frac{N}{2} - n_1} \binom{\frac{N}{2} - n_1}{n_2} \binom{\frac{N}{2} - n_2}{n_1}, \quad (3)$$

in the case of PBC, with an analogous expression for open boundary condition. For simplicity, we assumed N is even.

Using Hermiticity and the sublattice exchange symmetry, all matrix elements of H in the symmetric subspace can be found by examining only the $(H)_{(n_1, n_2)}^{(n_1-1, n_2)} = \langle (n_1-1, n_2) | H | (n_1, n_2) \rangle$ matrix elements. These can be found using the idea that for each configuration in (n_1, n_2) there are precisely n_1 ways to remove an excitation from sublattice 1. Accounting for normalisation and using the closed form Eq. (3) yields a remarkably simple effective Hamiltonian within \mathcal{K} :

$$(H)_{(n_1, n_2)}^{(n_1-1, n_2)} = \sqrt{\frac{n_1(\frac{N}{2} - n_1 - n_2)(\frac{N}{2} - n_1 - n_2 + 1)}{\frac{N}{2} - n_1}}. \quad (4)$$

IV. Properties of quasimodes

The quasimodes, or approximations to eigenstates, are formed by diagonalising the PXP Hamiltonian projected to \mathcal{K} , Eq. (4). Despite the apparent simplicity of the matrix elements, we are unaware of an analytical method to diagonalise Eq. (4) and we perform this step numerically. In Fig. 2(a) we compare the quasimodes against the exact eigenstates for system size $N=32$. For both the eigenstates and quasimodes we plot their mean energy and overlap with $|\mathbb{Z}_2\rangle$ state. $N+1$ scarred quasimodes, indicated with red crosses, stand out by closely matching the scarred eigenstates, which are responsible for the observed quantum revivals. These scarred quasimodes have previously been constructed via the FSA.¹⁰ In contrast, the present method yields a larger set of $O(N^2)$ quasimodes. The remaining quasimodes, indicated with the blue pluses in Fig. 2(a), also follow a regular pattern.

We measure the localisation of the quasimodes among energy eigenstates using participation ratio, $\text{PR} = \sum_E |\langle E | \phi_a \rangle|^4$, which represents the inverse of the number of eigenstates with which a state has ‘typical’ overlap. For random states this is $1/\mathcal{D}$, with \mathcal{D} the Hilbert space dimension. In Fig. 2(b) we plot the PR

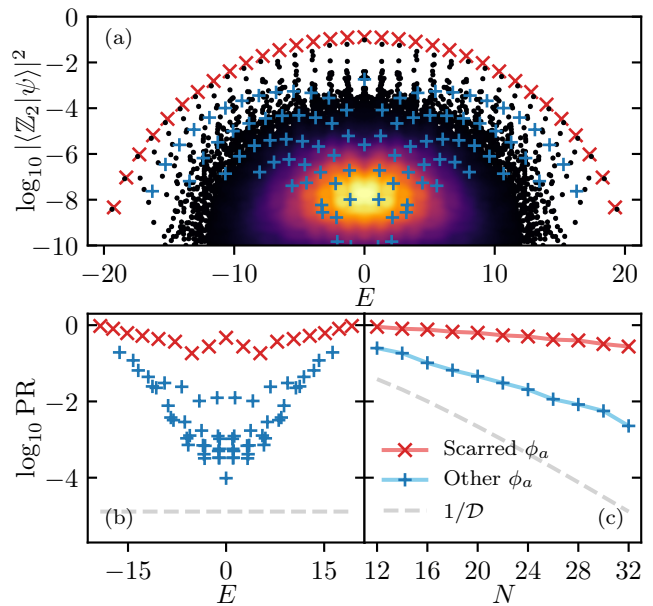


Figure 2. Quasimode properties. (a) Scatter plot showing energies of all eigenstates vs. their overlap with $|\mathbb{Z}_2\rangle$ state. Red crosses denote scarred quasimodes, blue pluses are the remaining quasimodes. Colour indicates the density of data points. (b), (c): Localisation of quasimodes in the energy eigenbasis. Plots show PR (see text) as a function of (b) energy E (for $N = 32$) and (c) system size N . In (c) we compare the scarred quasimode closest to $E = 0$ with the mean over the non-scarred quasimodes with $0 < E < \sqrt{N}$, all in the zero momentum sector. The scaling of PR is different for all scarred modes compared to the generic states (grey dashed line).

of all the quasimodes. The $N+1$ scarred quasimodes have very large PR compared to a typical random state, with appreciable overlap with only a small number of eigenstates. The remaining quasimodes are also significantly more localised than typical states. In Fig. 2(c) we show the scaling of PR with N , focusing on the scarred quasimode closest to the middle of the spectrum ($E = 0$) in the zero-momentum sector, alongside non-scarred quasimodes with energies $0 < E < \sqrt{N}$. This avoids the edges of the spectrum where the density of states is much smaller. From this we conclude that the scarred quasimodes are localised over a small number of eigenstates compared to the density of states.

Furthermore, the simple structure of the symmetric subspace allows us to characterise the errors in our eigenstate approximations beyond the limits of ED. We can calculate the energy variance matrix in the symmetric subspace, $\sigma_H^2 = \hat{\mathcal{K}}(H^2) - (\hat{\mathcal{K}}(H))^2$, where $\hat{\mathcal{K}}$ is a super-operator which projects linear operators on the full Hilbert space down to the symmetric subspace \mathcal{K} . It can be shown that the energy variance matrix is diagonal in the

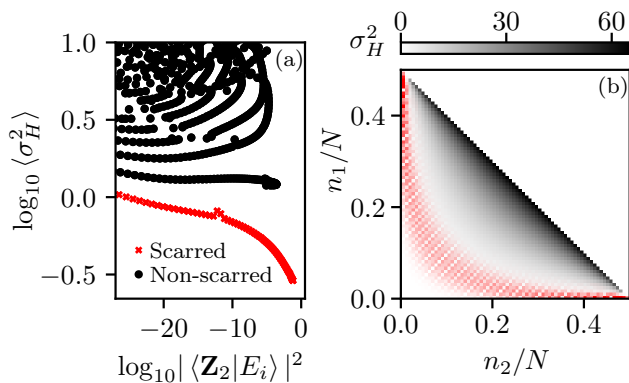


Figure 3. (a) Energy variance of the quasimodes for $N = 140$. Scarred quasimodes (red crosses) have low energy variance density compared to typical energy scales, indicating that the dynamics restricted to \mathcal{K} remains close to the exact evolution to relatively long times. (b) Energy variance in the symmetric basis, Eq. (2), as a function of scaled n_1 and n_2 . Superimposed (in red) is the probability distribution on n_1 and n_2 for a scarred quasimode in the middle of the spectrum (with $E \approx 27.28$).

symmetric basis and has the following closed form:⁷⁶

$$\sigma_H^2 = \frac{\hat{n}_1 \hat{n}_2 (\hat{n}_2 - 1)}{\left(\frac{N}{2} - \hat{n}_1 - 1\right) \left(\frac{N}{2} - \hat{n}_1\right)} + (1 \leftrightarrow 2), \quad (5)$$

where \hat{n}_1, \hat{n}_2 are the operators that count excitations on their respective sublattices, e.g., $\hat{n}_i |(n_1, n_2)\rangle = n_i |(n_1, n_2)\rangle$ for $i = 1, 2$.

As expected, among the quasimodes, we find that the scarred ones are those with the smallest energy variance, especially those that have high overlap with $|\mathbb{Z}_2\rangle$ state. This can be seen in Fig. 3(a), which shows the energy variance for individual quasimodes in system size $N=140$. The variance is linear in N , representing constant density of energy fluctuations, but for the scarred quasimodes it is much smaller than the typical energy scales. The average energy fluctuations in a quasimode is asymptotically given by $1/9$, while the same quantity restricted to scarred quasimodes is found numerically to be ≈ 0.0049 . This suggests that the time evolution approximated within this subspace will be reasonably accurate for local quantities such as local observable expectations for relatively long times. The typical scarred quasimode support can be visualised on an (n_1, n_2) triangle – see Fig. 3(b), which reveals that in these cases the quasimodes tend to “avoid” the region with n_1 and n_2 both large where the energy variance is high. This is analogous to the classical trajectory in the TDVP avoiding “high-leakage” regions of the phase space.¹¹

V. Quantum dynamics

Our construction of the quasimodes can also be used to approximate the dynamics of the system. This is illus-

trated in Fig. 4, which displays a comparison with ED as well as variational (TDVP) results, for a quench from the \mathbb{Z}_2 Rydberg crystal. TDVP approach is based on a restricted class \mathcal{M} of matrix product states $|\tilde{\Psi}(\theta, \phi)\rangle$ with bond dimension equal to 2, which can be parametrised using matrices^{9,11}

$$\mathcal{A}_i^{\circ} = \begin{pmatrix} \cos \frac{\theta_i}{2} & 0 \\ 1 & 0 \end{pmatrix}, \quad \mathcal{A}_i^{\bullet} = \begin{pmatrix} 0 & -ie^{i\phi_i} \sin \frac{\theta_i}{2} \\ 0 & 0 \end{pmatrix}, \quad (6)$$

where i labels the lattice sites or, in an infinite system, sites within a unit cell (for the $|\mathbb{Z}_2\rangle$ quench, $i = 1, 2$). The states are asymptotically normalised, $\langle \tilde{\Psi}(\theta, \phi) | \tilde{\Psi}(\theta, \phi) \rangle \rightarrow 1$, as $N \rightarrow \infty$.¹¹ The time evolution of the TDVP angles in Fig. 4 was obtained using the equations of motions for the infinite system.^{24,76}

The differences between the dynamics within \mathcal{K} and the TDVP dynamics on \mathcal{M} can be seen clearly in Fig. 4(a), which shows the von Neumann entropy for an equal bipartition of the system. This quantity, although non-local, can also be efficiently calculated using the present method.⁷⁶ We observe that entropy captures the differences between approximation schemes well before the relaxation time set by the energy variance. In contrast, local quantities such as local expectation values are very consistent – see Fig. 4(b) which shows the density of Rydberg excitations in the system, $\langle n/N \rangle$. The accuracy of these different methods can be assessed using co-moving fidelity densities between pairs of evolutions, such as $\frac{1}{N} \log (|\langle \psi_{\text{ED}}(t) | \psi_{\mathcal{K}}(t) \rangle|^2)$. Both the TDVP and symmetric subspace approaches generate a very low error density. The dynamics in the symmetric subspace has been simulated in large system sizes (for $N \leq 720$ ⁷⁶), and the results are consistent with the revivals of the Néel states becoming perfect in the thermodynamic limit. However, there is a slight deviation from the TDVP orbit,¹¹ in that there is no perfect state transfer between $|\bullet\bullet\bullet\dots\rangle$ and the Néel state with the two sublattices flipped, $|\bullet\circ\circ\dots\rangle$.

The co-moving fidelities in Fig. 4(c) underscore there is a curious similarity between the evolutions within TDVP and symmetric subspace \mathcal{K} . The variational class of states considered in the TDVP approach can be viewed as a Gutzwiller projection of spin coherent states with a unit cell of two sites, where the projector eliminates nearest neighbour excitations.^{9,11,24} The states in this subspace \mathcal{M} are parametrised by two angles which represent probabilities for a site of each sublattice to hold an excitation. Recall that the basis for \mathcal{K} consisted of states with definite occupations numbers for each sublattice. In this sense, there is a direct relationship between the two subspaces, reminiscent of the relationship between canonical and grand canonical ensembles in statistical mechanics. More formally, it can be proven that the linear span of \mathcal{M} is equal to the symmetric subspace \mathcal{K} , for every fixed system size N .⁷⁶ This implies that the dynamics within \mathcal{K} has a leakage rate, or instantaneous error, which is bounded above by that of the TDVP evolution. Next we will investigate this connection in more detail and show how \mathcal{K} and \mathcal{M} are related by quantisation.

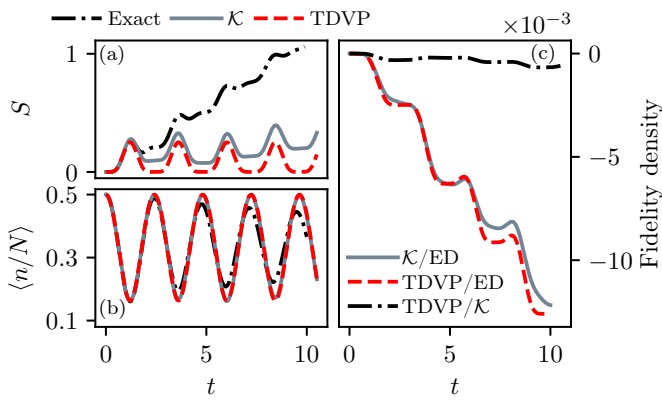


Figure 4. Dynamics for $N = 32$. (a) Entanglement entropy following a quench for the full quantum dynamics, the dynamics projected into \mathcal{K} , and the TDVP dynamics on \mathcal{M} . The entropy growth shows that for \mathcal{K} , the initial state does not recur exactly leaving some residual entropy compared to the more weakly entangled dynamics on \mathcal{M} . (b) Local observables following the quench are well reproduced. Both TDVP and \mathcal{K} subspace approximations fail to capture a slow decay in the oscillations for $t \gtrsim 5$. (c) Pairwise comparisons between the exact dynamics, projected dynamics on \mathcal{K} and TDVP dynamics on \mathcal{M} . This illustrates that the dynamics on \mathcal{K} is always more accurate than TDVP on \mathcal{M} .

VI. Quantisation of periodic orbits and the correspondence principle

Our final step is to establish a correspondence between \mathcal{K} and TDVP. The latter is typically conceived as a variational approximation method – how do we reinterpret it as a classical limit? Conversely, how can we best quantise this classical system, given that quantisation is often a non-unique recipe? These questions are conveniently addressed in a path integral framework. Thus, we first carefully formulate the path integral over our constrained space before arriving at the correspondence principle that relates \mathcal{M} and \mathcal{K} .

A. The variational principle and dequantisation

A path integral over a classical system is usually used to define a quantum propagator which associates amplitudes to pairs of path endpoints. This propagator may be viewed as a linear operator over the span of the classical space. However, in the present case, we follow a reverse procedure: we use the path-integral formulation to “dequantise” a system by writing its propagator as a path integral and then take its constituent classical state space and action functional as defining a classical system. When the TDVP state space furnishes a resolution of the identity, the TDVP retraction is equivalent to such a dequantisation.⁷⁶ This process provides a correspondence between a classical system such as \mathcal{M} and a quantum system in its linear span – for \mathcal{M} , this is the

Rayleigh-Ritz projection of the dynamics in the symmetric subspace \mathcal{K} . This is clearly the most natural outcome, as it meets our expectation that the different representations of quantum mechanics — i.e. position, momentum or coherent-state — are precisely that: representations of the same object. If the same variational principle is taken for restricting to a vector subspace, such as our symmetric subspace \mathcal{K} , then the Rayleigh-Ritz method is exactly recovered. It is natural that both the quantised and dequantised system satisfy this same kind of variational optimality.

Crucially, the prescription above relies on being able to associate a measure μ to some family of paths. This can be achieved by equipping the classical state space with an integration measure, forming a structure we will refer to as a *frame*.⁷⁷ This structure is characterised by the frame operator,

$$S_\mu = \int_{\mathcal{M}} d\mu_{\theta,\phi} |\tilde{\Psi}(\theta,\phi)\rangle \langle \tilde{\Psi}(\theta,\phi)|, \quad (7)$$

using the parametrisation of states in Eq. (6). For (\mathcal{M}, μ) to constitute a genuine frame, S_μ must be bounded and positive definite. It is this operator which must reproduce the identity to have a well-defined quantisation. Unfortunately, our state space \mathcal{M} does not come with a natural choice of μ , unlike many of the familiar manifolds of quantum states, such as spin coherent states and matrix product states,⁷⁸ where μ is simply given by the Haar measure for a transitive group action.⁷⁹ Even a measure which works for the space of constrained coherent states where every site has independent variables (θ_j, ϕ_j) , found in Ref. 11, does not survive when these are restricted to two-site periodicity.

The strategy we will follow is to start from a measure that produces a frame over \mathcal{M} which is at least reasonably well-behaved, although it may not resolve the identity. The corresponding frame operator S_μ will turn out to be bounded and positive definite for all finite N , albeit merely positive semidefinite in the limit $N \rightarrow \infty$. This can then be used to construct a transformed state space, $\tilde{\mathcal{M}}$, that *does* resolve the identity, and thus quantise naturally. Formally, we construct this new frame $(\tilde{\mathcal{M}}, \mu)$ from our existing one by replacing the states attached to each point of the space according to the linear action,

$$|\tilde{\Psi}\rangle \mapsto S_\mu^{-1/2} |\tilde{\Psi}\rangle. \quad (8)$$

We refer to this as a frame transformation in analogy to a basis transformation. This process is well defined whenever S_μ is bounded and positive definite, and the corresponding frame operator is the identity operator. In this case, the thermodynamic limit can be regularised such that it quantises naturally to a space with only some “non-physical” states removed. The removal of non-physical states is justified because, by construction, \mathcal{M} is meant to be effective at describing the Néel state quench, while in other parts of the phase space the leakage rate or geometric error may be large.^{11,24} For finite sizes, we will show that the transformed space is a

moral equivalent to \mathcal{M} , in the sense that they are highly similar around the “good” trajectories, while potentially disagreeing about the “bad” trajectories. Furthermore, we will show the differences between the two shrink as N increases, until in the thermodynamic limit they are equivalent almost everywhere.

Our starting point is the gauged coherent state parametrisation for \mathcal{M} , Eq. (6), and we want to find a measure such that S_μ is bounded. The choice of measure is to an extent arbitrary, since its details will be transformed away later, but the challenge of ensuring that S_μ is bounded can be understood from the following heuristic argument. Consider the expectation value of S_μ for a point x of \mathcal{M} . A contribution to this integral will be significant if it is not too distinguishable from x , and therefore the integral can be estimated by the volume of the “fuzzy” set indistinguishable from x . For almost all x and as N increases, the fuzzy neighbourhood retracts around x to a point, with a typical fuzzy size $O(1/\sqrt{N})$. This phenomena also occurs on the manifold of spin-coherent states with increasing spin.⁸⁰ For x along the edges (i.e. $\theta_1 = \pi$), however, it retracts to a line, with a typical fuzzy width $O(1/\sqrt{N})$. The line-like contributions to S_μ appear at a higher order in N , due to their different volume scaling, thus spoiling a bounded positive-definite limit. This issue can be avoided by adopting for our measure

$$d\mu = \left(\frac{N+1}{4\pi}\right)^2 \prod_{i=1,2} d\theta_i d\phi_i \sin\theta_i \cos^2\frac{\theta_i}{2}. \quad (9)$$

Relative to the product of spherical measures, the additional $\cos^2\frac{\theta_i}{2}$ is chosen to vanish rapidly enough at the edges of the phase space that the singularity is removed.

We proceed by examining matrix elements of S_μ in the symmetric basis of \mathcal{K} . Only the diagonal matrix elements $(S_\mu)_{n_1, n_2} = \langle (n_1, n_2) | S_\mu | (n_1, n_2) \rangle$ are non-zero. For periodic boundary conditions these are

$$(S_\mu)_{n_1, n_2} = \frac{\frac{N}{2}(\frac{N}{2}+1)^2(\frac{N}{2}-n_1-n_2)(\frac{N}{2}-n_1-n_2+1)^2}{(\frac{N}{2}-n_1)^{(3)}(\frac{N}{2}-n_2)^{(3)}}, \quad (10)$$

where $(x)^{(n)}$ is the rising factorial or Pochhammer polynomial.⁸¹ As mentioned previously, we see that the frame operator S_μ is bounded and positive definite for every finite N , but it is merely positive semidefinite in the $N \rightarrow \infty$ limit. The inverse is only ill conditioned near the diagonal in the (n_1, n_2) plane, but this subspace dynamically decouples from the rest of \mathcal{K} since the Hamiltonian matrix elements involving this subspace vanish asymptotically. Moreover, when represented on \mathcal{M} , it concentrates for large N around the corners, $(\theta_1, \theta_2) = (\pm\pi, \pm\pi)$, which are not physically relevant for the Néel state quench, besides being measure zero. We can form a convergent series for the inverse by regularising it with a scalar, $(S_\mu + \epsilon)^{-1/2}$, which has a projector onto \mathcal{K} with the decoupled space removed for its limit. This allows us to

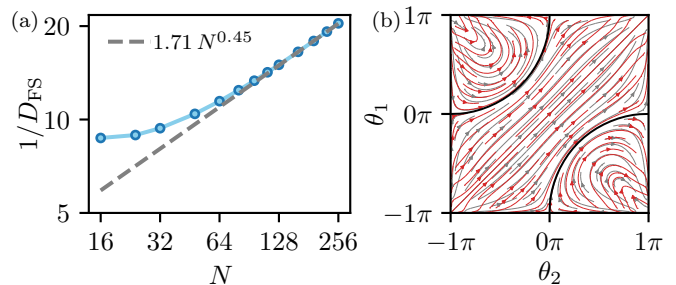


Figure 5. (a) Fubini-Study distance D_{FS} between original \mathcal{M} and transformed $\overline{\mathcal{M}}$ state spaces, averaged over the phase-space with measure μ . (b) Illustration of the integral curves of (red) the frame-transformed dynamics and (grey) the original dynamical system, for $N = 128$. The flows are highly similar except towards the corners. The black line shows the evolution following a Néel state quench in the transformed system.

define the frame-transformed space $\overline{\mathcal{M}}$ even in the thermodynamic limit.

We find that almost all of the phase space is left essentially unaffected by the frame transformation in the thermodynamic limit.⁷⁶ This occurs because the frame operator S_μ is a function of the densities n_1/N , n_2/N , with a positive radius of convergence, except in the thermodynamic limit when approaching the diagonal in the (n_1, n_2) plane. The fluctuations in the density observables decay as $O(1/\sqrt{N})$ over almost all of \mathcal{M} because the correlation length of connected correlation functions only diverges towards the corners where the states are dominated by configurations composed of a small number of large Néel domains. This means that S_μ asymptotically acts essentially as a scalar on each of the points of \mathcal{M} ,⁷⁶ and can therefore be absorbed into the measure. Asymptotically, the two state spaces, \mathcal{M} and $\overline{\mathcal{M}}$, are equal almost everywhere, and their convergence is numerically demonstrated in Fig. 5(a), which shows the Fubini-Study metric or Bures distance⁸² D_{FS} — which measures the angle between two states as projective rays — averaged over the phase space. In the large- N limit, we find $D_{\text{FS}} \sim 1/\sqrt{N}$, which supports the asymptotic equivalence between \mathcal{M} and $\overline{\mathcal{M}}$. The change in measure is unable to affect the behaviour of the classical dynamical system, which can be formulated entirely independent of the measure.

Wherever the fluctuations are small, the frame operators acts approximately as a scalar with small corrections due to density fluctuations. Hence, even for finite system sizes, the transformed space is very similar to the original space except around regions of the phase-space which are considered non-physical. This is shown in Fig. 5 (b) for $N=128$, where the grey lines are the original dynamical system and the red lines are the frame-transformed dynamics. The vector fields are for finite-sized systems and are calculated from the action principal represented in the symmetric basis for \mathcal{K} . This method avoids numer-

ical instability found in the canonical treatment⁵¹ around singularities in the tangent-basis Gram matrix. We observe in Fig. 5 (b) that the Hamiltonian vector fields agree around the good trajectories and diverge from one another on approaching the corners. The black line is an integral curve for the frame-transformed system starting from the Néel state, thus showing that the trajectory which underlies the quantum scar dynamics is retained.

To summarise, we have shown there is a measure which quantises the original space \mathcal{M} to \mathcal{K} , in the thermodynamic limit and after removing the physically-irrelevant subspace. This was achieved by constructing a sequence of transformed spaces for finite sizes which has a common $N \rightarrow \infty$ limit as the original space. Each finite N transformed space quantises naturally to the Hilbert space \mathcal{K} examined in the previous sections, in which many quantities of interest may be calculated efficiently. Even for finite system sizes, the transformed space is very similar to the original space except around regions of the phase-space which are considered non-physical.

B. Physical interpretation of quasimodes

Having provided a quantisation–dequantisation correspondence between the classical TDVP system and the symmetric subspace \mathcal{K} , we now turn to the consequences for our interpretation of individual quasimodes, and by extension the exact eigenstates. We will show that our scarred quasimodes can be viewed as standing waves localised around the Néel state trajectory, making contact with the the phenomena which inspired the term quantum scar in quantum billiard systems. In these systems, it was found that some eigenfunctions anomalously localise around isolated periodic orbits,¹ leading to the picture that the classical trajectory is “imprinted” upon the quantum states, giving rise to wavefunction scarring.

First, we will show how the quasimodes can be viewed as wavefunctions. The frames constructed in the previous section, which resolve the identity, allow us to analyse a quantum state $|\psi\rangle \in \mathcal{K}$ through the inner-product map:

$$\psi(\theta, \phi) = \langle \tilde{\Psi}(\theta, \phi) | S_\mu^{-1/2} |\psi\rangle, \quad (11)$$

$$|\psi\rangle = \int_{\mathcal{M}} d\mu_{\theta, \phi} \psi(\theta, \phi) S_\mu^{-1/2} |\tilde{\Psi}(\theta, \phi)\rangle. \quad (12)$$

This mapping allows us to form a wavefunction representation, $\psi(\theta, \phi)$, and, conversely, to recover the quantum state from that representation. This serves as a phase-space analogue to a wavefunction, which in the usual Schrödinger picture would be defined only on a Lagrangian submanifold such as configuration space. Squaring this wavefunction creates an analogue to the Husimi Q-representation which is a quasi-probability distribution rather than a true probability distribution because its events are not disjoint.⁸⁰

We restrict attention to a Lagrangian section with $\phi_a = 0$, as this typically loses no information and the two-dimensional space is better suited for visualisation.²⁴ The

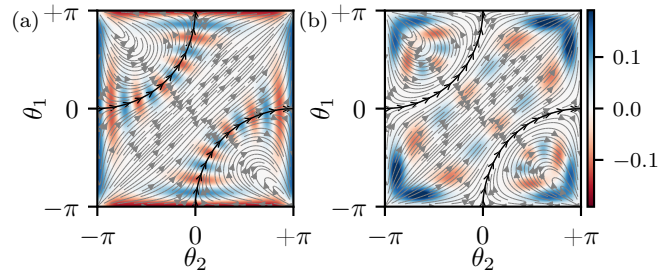


Figure 6. Viewing a selected (a) scarred and (b) non-scarred quasimode as wavefunctions over θ_1 and θ_2 for $N=128$. Colour scale represents the real part of the wavefunction. Scarred quasimodes concentrate around the classical periodic orbits demonstrating quantum scarring. The phase of the wavefunction winds along the trajectory, and this winding number is related to the approximately equally spaced energies of the quasimodes. The other quasimodes avoid this periodic trajectory, due to orthogonality, and concentrate around the trajectories with the corners of the square for endpoints.

real part of the wavefunction representation in Eq. (11) is shown in Fig. 6, for an illustrative example of a scarred quasimode (a) and one of the remaining quasimodes (b), for $N=128$. The scarred quasimodes are found to concentrate around the Néel classical trajectory in a manner strikingly reminiscent of wavefunction scarring in the quantum billiards problem. The classical trajectory shown by the black line in Fig. 6 is for the thermodynamic limit. In Fig. 6(a) we observe that the wavefunction spreads out towards the boundary and becomes completely delocalised at the edges, $\theta_i = \pm\pi$, where the points are indistinguishable in the transverse direction. Following the classical trajectory, the phase of the wavefunction winds, and integrality of this winding number leads to their approximately equal spacing in energy. We recognise this behaviour from quantisation of regular trajectories:⁸³ in the old quantum theory, this underpins Sommerfeld-Wilson quantisation and leads to the de Broglie standing-wave condition for the Bohr model. These features are inherited by the scarred exact eigenstates given their strong overlap with the quasimodes.

In contrast, the non-scarred quasimodes are typically found around the orbits connecting corners of the manifold – see Fig. 6(b). The corners represent the zero vector in the quantum picture, around which the geometric error is large. This may account for the increased energy variance and energy delocalisation found previously in such quasimodes.

We note a dissimilarity between our result in Fig. 6 and wavefunction scarring in the fact that the phase-space section is entirely regular. It cannot exhibit chaos because a symmetry argument leaves the two-dimensional $\phi_a=0$ section dynamically invariant.¹¹ The non-scarred quasimodes are distinguished from those we have called scarred not by a chaotic nature but because they do not appear to survive the injection into the full Hilbert space. Because of the greater variational errors en-

countered along the other trajectories, we suggest that the variational space could be increased with additional parameters in such a way that the bad trajectories lose stability – leading to the emergence of classical chaos. The Néel trajectory ought to remain regular, producing a phase-space which is mixed or perhaps with isolated regular trajectories.²⁴

VII. Conclusions

We have introduced a symmetric subspace \mathcal{K} which allows for a simple construction of quasimodes in the Rydberg atom model. We showed that these quasimodes are well-localised in the energy eigenbasis and have greatly suppressed energy fluctuations, thereby making them excellent approximations to both the exact eigenstates and the quench dynamics. The simplicity of this approach allowed us to obtain closed form results for many important quantities and our method can be easily extended to account for various perturbations to the PXP model that have been considered in the literature.^{12,14,55} Moreover, we expect the analogue of subspace \mathcal{K} to be particularly useful in studying two-dimensional scarred models,^{39,84,85} and in describing dynamics in other types of constrained models, e.g., quantum dimer models,⁸⁶ whose ground states have a similar “symmetrised” structure at Rokhsar-Kivelson points.⁸⁷

We have argued that our subspace \mathcal{K} can be interpreted as a “requantisation” of the variational classical limit,¹¹ when quantum fluctuations are restored to all orders. This reveals the TDVP classical system is formed of two approximations, one of which is a mean-field type

approximation and another which is the classical limit. Using finite size scaling, we showed that the wavefunction revivals survive in the thermodynamic limit in the mean-field regime, but the state transfer between the two Néel state is no longer perfect. This means that the TDVP periodic trajectories are robust to the addition of quantum fluctuations.

These results allow us to complete the analogy between the wavefunction scarring in the PXP model and the single-particle quantum systems. The one outstanding challenge for making contact between the quasimodes and rigorous results on exact eigenstates is the exponential many-body density of states. The subspace constructed here is naturally related to a large approximate symmetry action which shuffles the lattice sites, within the even and odd sublattices – this could provide a way to control the density of states in order to rigorously prove the existence of quantum non-unique ergodicity in the thermodynamic limit of the Rydberg atom chain.

VIII. Acknowledgements

We thank Alexios Michailidis for useful discussions. We acknowledge support by EPSRC grants EP/R020612/1, EP/R513258/1 and EP/M50807X/1. Statement of compliance with EPSRC policy framework on research data: This publication is theoretical work that does not require supporting research data. This work benefited from participation at KITP Follow-Up programme, supported by the National Science Foundation under Grant No. NSF PHY-1748958.

¹ Eric J Heller, “Bound-state eigenfunctions of classically chaotic Hamiltonian systems: Scars of periodic orbits,” *Phys. Rev. Lett.* **53**, 1515–1518 (1984).
² E. J. Heller, “Wavepacket dynamics and quantum chaos,” in *Chaos and quantum physics*, Vol. 52 (North-Holland: Amsterdam, 1991).
³ Michael Victor Berry, “Quantum scars of classical closed orbits in phase space,” *Proc. R. Soc. Lond. A* **423**, 219–231 (1989).
⁴ E.J. Heller, *The Semiclassical Way to Dynamics and Spectroscopy* (Princeton University Press, 2018).
⁵ Niels Bohr, “The correspondence principle (1918–1923),” in *Niels Bohr Collected Works*, Vol. 3 (Amsterdam: North-Holland Publishing, 1976).
⁶ Steve Zelditch, “Note on quantum unique ergodicity,” *Proc. Am. Math. Soc.* **132**, 1869–1873 (2004).
⁷ Patrick W O’Connor and Eric J Heller, “Quantum localization for a strongly classically chaotic system,” *Phys. Rev. Lett.* **61**, 2288–2291 (1988).
⁸ Andrew Hassell, “Ergodic billiards that are not quantum unique ergodic,” *Ann. Math.* **171**, 605–618 (2010).
⁹ Hannes Bernien, Sylvain Schwartz, Alexander Keesling, Harry Levine, Ahmed Omran, Hannes Pichler, Soon-

won Choi, Alexander S Zibrov, Manuel Endres, Markus Greiner, Vladan Vuletić, and Mikhail D Lukin, “Probing many-body dynamics on a 51-atom quantum simulator,” *Nature* **551**, 579–584 (2017).
¹⁰ C J Turner, A A Michailidis, D A Abanin, M Serbyn, and Z Papić, “Weak ergodicity breaking from quantum many-body scars,” *Nat. Phys.* **14**, 745–749 (2018).
¹¹ Wen Wei Ho, Soonwon Choi, Hannes Pichler, and Mikhail D Lukin, “Periodic orbits, entanglement, and quantum many-body scars in constrained models: Matrix product state approach,” *Phys. Rev. Lett.* **122**, 040603 (2019).
¹² Soonwon Choi, Christopher J Turner, Hannes Pichler, Wen Wei Ho, Alexios A Michailidis, Zlatko Papić, Maksym Serbyn, Mikhail D Lukin, and Dmitry A Abanin, “Emergent SU(2) dynamics and perfect quantum many-body scars,” *Phys. Rev. Lett.* **122**, 220603 (2019).
¹³ Cheng-Ju Lin and Olexei I. Motrunich, “Exact quantum many-body scar states in the Rydberg-blockaded atom chain,” *Phys. Rev. Lett.* **122**, 173401 (2019).
¹⁴ Vedika Khemani, Chris R. Laumann, and Anushya Chandran, “Signatures of integrability in the dynamics of Rydberg-blockaded chains,” *Phys. Rev. B* **99**, 161101

- (2019).
- 15 Kieran Bull, Jean-Yves Desaulès, and Zlatko Papić, “Quantum scars as embeddings of weakly ”broken” Lie algebra representations,” *Phys. Rev. B* **101**, 165139 (2020).
 - 16 Daniel K Mark, Cheng-Ju Lin, and Olexei I Motrunich, “Exact eigenstates in the Lesanovsky model, proximity to integrability and the PXP model, and approximate scar states,” *Phys. Rev. B* **101**, 094308 (2020).
 - 17 Marton Kormos, Mario Collura, Gabor Takács, and Pasquale Calabrese, “Real-time confinement following a quantum quench to a non-integrable model,” *Nat. Phys.* **13**, 246 (2016).
 - 18 Andrew J. A. James, Robert M. Konik, and Neil J. Robinson, “Nonthermal states arising from confinement in one and two dimensions,” *Phys. Rev. Lett.* **122**, 130603 (2019).
 - 19 Neil J. Robinson, Andrew J. A. James, and Robert M. Konik, “Signatures of rare states and thermalization in a theory with confinement,” *Phys. Rev. B* **99**, 195108 (2019).
 - 20 Oskar Vafek, Nicolas Regnault, and B. Andrei Bernevig, “Entanglement of exact excited eigenstates of the Hubbard model in arbitrary dimension,” *SciPost Phys.* **3**, 043 (2017).
 - 21 Sanjay Moudgalya, Nicolas Regnault, and B. Andrei Bernevig, “Entanglement of exact excited states of Affleck-Kennedy-Lieb-Tasaki models: Exact results, many-body scars, and violation of the strong eigenstate thermalization hypothesis,” *Phys. Rev. B* **98**, 235156 (2018).
 - 22 Thomas Iadecola and Marko Žnidarič, “Exact localized and ballistic eigenstates in disordered chaotic spin ladders and the Fermi-Hubbard model,” *Phys. Rev. Lett.* **123**, 036403 (2019).
 - 23 Seulgi Ok, Kenny Choo, Christopher Mudry, Claudio Castelnovo, Claudio Chamon, and Titus Neupert, “Topological many-body scar states in dimensions one, two, and three,” *Phys. Rev. Research* **1**, 033144 (2019).
 - 24 A. A. Michailidis, C. J. Turner, Z. Papić, D. A. Abanin, and M. Serbyn, “Slow quantum thermalization and many-body revivals from mixed phase space,” *Phys. Rev. X* **10**, 011055 (2020).
 - 25 Michael Schecter and Thomas Iadecola, “Weak ergodicity breaking and quantum many-body scars in spin-1 XY magnets,” *Phys. Rev. Lett.* **123**, 147201 (2019).
 - 26 Asmi Halder, Diptiman Sen, Roderich Moessner, and Arnab Das, “Scars in strongly driven Floquet matter: resonance vs emergent conservation laws,” (2019), [arXiv:1909.04064 \[cond-mat.other\]](https://arxiv.org/abs/1909.04064).
 - 27 Bhaskar Mukherjee, Sourav Nandy, Arnab Sen, Diptiman Sen, and K. Sengupta, “Collapse and revival of quantum many-body scars via Floquet engineering,” *Phys. Rev. B* **101**, 245107 (2020).
 - 28 Sho Sugiura, Tomotaka Kuwahara, and Keiji Saito, “Many-body scar state intrinsic to periodically driven system: Rigorous results,” (2019), [arXiv:1911.06092 \[cond-mat.stat-mech\]](https://arxiv.org/abs/1911.06092).
 - 29 Sanjay Moudgalya, B. Andrei Bernevig, and Nicolas Regnault, “Quantum many-body scars in a Landau level on a thin torus,” (2019), [arXiv:1906.05292 \[cond-mat.str-el\]](https://arxiv.org/abs/1906.05292).
 - 30 Thomas Iadecola and Michael Schecter, “Quantum many-body scar states with emergent kinetic constraints and finite-entanglement revivals,” *Phys. Rev. B* **101**, 024306 (2020).
 - 31 Ana Hudomal, Ivana Vasić, Nicolas Regnault, and Zlatko Papić, “Quantum scars of bosons with correlated hopping,” *Communications Physics* **3**, 1–12 (2020).
 - 32 Shriya Pai and Michael Pretko, “Dynamical scar states in driven fracton systems,” *Phys. Rev. Lett.* **123**, 136401 (2019).
 - 33 Kieran Bull, Ivar Martin, and Z. Papić, “Systematic construction of scarred many-body dynamics in 1D lattice models,” *Phys. Rev. Lett.* **123**, 030601 (2019).
 - 34 Berislav Buča, Joseph Tindall, and Dieter Jaksch, “Non-stationary coherent quantum many-body dynamics through dissipation,” *Nature Communications* **10**, 1730 (2019).
 - 35 J. Tindall, B. Buča, J. R. Coulthard, and D. Jaksch, “Heating-induced long-range η pairing in the Hubbard model,” *Phys. Rev. Lett.* **123**, 030603 (2019).
 - 36 Naoyuki Shibata, Nobuyuki Yoshioka, and Hoshio Katsura, “Onsager’s scars in disordered spin chains,” *Phys. Rev. Lett.* **124**, 180604 (2020).
 - 37 Sanjay Moudgalya, Abhinav Prem, Rahul Nandkishore, Nicolas Regnault, and B. Andrei Bernevig, “Thermalization and its absence within Krylov subspaces of a constrained Hamiltonian,” (2019), [arXiv:1910.14048 \[cond-mat.str-el\]](https://arxiv.org/abs/1910.14048).
 - 38 Hongzheng Zhao, Joseph Vovrosh, Florian Mintert, and Johannes Knolle, “Quantum many-body scars in optical lattices,” *Phys. Rev. Lett.* **124**, 160604 (2020).
 - 39 Kyungmin Lee, Ronald Melendrez, Arijeet Pal, and Hitesh J. Changlani, “Exact three-colored quantum scars from geometric frustration,” *Phys. Rev. B* **101**, 241111 (2020).
 - 40 Daniel K Mark, Cheng-Ju Lin, and Olexei I Motrunich, “Unified structure for exact towers of scar states in the Affleck-Kennedy-Lieb-Tasaki and other models,” *Physical Rev. B* **101**, 195131 (2020).
 - 41 Sanjay Moudgalya, Edward O’Brien, B. Andrei Bernevig, Paul Fendley, and Nicolas Regnault, “Large classes of quantum scarred Hamiltonians from matrix product states,” (2020), [arXiv:2002.11725 \[cond-mat.str-el\]](https://arxiv.org/abs/2002.11725).
 - 42 David Villaseñor, Saúl Pilatowsky-Cameo, Miguel A Bastarrachea-Magnani, Sergio Lerma, Lea F Santos, and Jorge G Hirsch, “Quantum vs classical dynamics in a spin-boson system: manifestations of spectral correlations and scarring,” *New Journal of Physics* (2020).
 - 43 Sanjay Moudgalya, Nicolas Regnault, and B. Andrei Bernevig, “Eta-pairing in Hubbard models: From spectrum generating algebras to quantum many-body scars,” (2020), [arXiv:2004.13727 \[cond-mat.str-el\]](https://arxiv.org/abs/2004.13727).
 - 44 Daniel K. Mark and Olexei I. Motrunich, “Eta-pairing states as true scars in an extended Hubbard model,” (2020), [arXiv:2004.13800 \[cond-mat.str-el\]](https://arxiv.org/abs/2004.13800).
 - 45 Bart van Voorden, Ji Min, and Kareljan Schoutens, “Quantum many-body scars in transverse field Ising ladders and beyond,” (2020), [arXiv:2003.13597 \[cond-mat.str-el\]](https://arxiv.org/abs/2003.13597).
 - 46 Kaoru Mizuta, Kazuaki Takasan, and Norio Kawakami, “Exact Floquet quantum many-body scars under Rydberg blockade,” (2020), [arXiv:2004.04431 \[cond-mat.stat-mech\]](https://arxiv.org/abs/2004.04431).
 - 47 Oliver Hart, Giuseppe De Tomasi, and Claudio Castelnovo, “The random quantum comb: from compact localized states to many-body scars,” (2020), [arXiv:2005.03036 \[cond-mat.str-el\]](https://arxiv.org/abs/2005.03036).
 - 48 Wil Kao, Kuan-Yu Li, Kuan-Yu Lin, Sarang Gopalakrishnan, and Benjamin L. Lev, “Creating quantum many-body scars through topological pumping of a 1D dipolar gas,” (2020), [arXiv:2002.10475 \[cond-mat.quant-gas\]](https://arxiv.org/abs/2002.10475).

- ⁴⁹ Igor Lesanovsky and Hosho Katsura, “Interacting Fibonacci anyons in a Rydberg gas,” *Phys. Rev. A* **86**, 041601 (2012).
- ⁵⁰ Paul Fendley, K. Sengupta, and Subir Sachdev, “Competing density-wave orders in a one-dimensional hard-boson model,” *Phys. Rev. B* **69**, 075106 (2004).
- ⁵¹ P Kramer and M Saraceno, *Geometry of the Time-Dependent Variational Principle in Quantum Mechanics*, Lecture Notes in Physics, Vol. 140 (Springer-Verlag, Berlin Heidelberg, 1981).
- ⁵² Jutho Haegeman, J. Ignacio Cirac, Tobias J. Osborne, Iztok Pižorn, Henri Verschelde, and Frank Verstraete, “Time-dependent variational principle for quantum lattices,” *Phys. Rev. Lett.* **107**, 070601 (2011).
- ⁵³ Eyal Levitan, Frank Pollmann, Jens H. Bardarson, David A. Huse, and Ehud Altman, “Quantum thermalization dynamics with matrix-product states,” (2017), [arXiv:1702.08894 \[cond-mat.stat-mech\]](https://arxiv.org/abs/1702.08894).
- ⁵⁴ A. Hallam, J. G. Morley, and A. G. Green, “The Lyapunov spectra of quantum thermalisation,” *Nature Communications* **10**, 2708 (2019).
- ⁵⁵ C J Turner, A A Michailidis, D A Abanin, M Serbyn, and Zlatko Papić, “Quantum scarred eigenstates in a Rydberg atom chain: Entanglement, breakdown of thermalization, and stability to perturbations,” *Phys. Rev. B* **98**, 12 (2018).
- ⁵⁶ Yochai Werman, “Quantum chaos in a Rydberg atom system,” (2020), [arXiv:2001.06110 \[quant-ph\]](https://arxiv.org/abs/2001.06110).
- ⁵⁷ VEDIKA Khemani and RAHUL NANDKISHORE, “Local constraints can globally shatter Hilbert space: a new route to quantum information protection,” (2019), [arXiv:1904.04815 \[cond-mat.stat-mech\]](https://arxiv.org/abs/1904.04815).
- ⁵⁸ Pablo Sala, Tibor Rakovszky, Ruben Verresen, Michael Knap, and Frank Pollmann, “Ergodicity-breaking arising from Hilbert space fragmentation in dipole-conserving Hamiltonians,” *Phys. Rev. X* **10**, 011047 (2020).
- ⁵⁹ VEDIKA Khemani, Michael Hermele, and RAHUL M. NANDKISHORE, “Localization from shattering: higher dimensions and physical realizations,” (2019), [arXiv:1910.01137 \[cond-mat.stat-mech\]](https://arxiv.org/abs/1910.01137).
- ⁶⁰ Sthitadhi Roy and Achilleas Lazarides, “Strong ergodicity breaking due to local constraints in a quantum system,” *Phys. Rev. Research* **2**, 023159 (2020).
- ⁶¹ Zhi-Cheng Yang, Fangli Liu, Alexey V Gorshkov, and Thomas Iadecola, “Hilbert-space fragmentation from strict confinement,” *Phys. Rev. Lett.* **124**, 207602 (2020).
- ⁶² Nicola Pancotti, Giacomo Giudice, J Ignacio Cirac, Juan P Garrahan, and Mari Carmen Bañuls, “Quantum East model: Localization, nonthermal eigenstates, and slow dynamics,” *Phys. Rev. X* **10**, 021051 (2020).
- ⁶³ J. M. Deutsch, “Quantum statistical mechanics in a closed system,” *Phys. Rev. A* **43**, 2046 (1991).
- ⁶⁴ Mark Srednicki, “Chaos and quantum thermalization,” *Phys. Rev. E* **50**, 888 (1994).
- ⁶⁵ Luca D’Alessio, Yariv Kafri, Anatoli Polkovnikov, and Marcos Rigol, “From quantum chaos and eigenstate thermalization to statistical mechanics and thermodynamics,” *Adv. Phys.* **65**, 239 (2016).
- ⁶⁶ Christian Gogolin and Jens Eisert, “Equilibration, thermalisation, and the emergence of statistical mechanics in closed quantum systems,” *Rep. Prog. Phys.* **79**, 056001 (2016).
- ⁶⁷ Denis M Basko, Igor L Aleiner, and Boris L Altshuler, “Metal-insulator transition in a weakly interacting many-electron system with localized single-particle states,” *Annals of physics* **321**, 1126–1205 (2006).
- ⁶⁸ Maksym Serbyn, Zlatko Papić, and Dmitry A Abanin, “Local conservation laws and the structure of the many-body localized states,” *Phys. Rev. Lett.* **111**, 127201 (2013).
- ⁶⁹ David A. Huse, Rahul Nandkishore, and Vadim Oganesyan, “Phenomenology of fully many-body-localized systems,” *Phys. Rev. B* **90**, 174202 (2014).
- ⁷⁰ Bill Sutherland, *Beautiful models: 70 years of exactly solved quantum many-body problems* (World Scientific Publishing Company, 2004).
- ⁷¹ Naoto Shiraishi and Takashi Mori, “Systematic construction of counterexamples to the eigenstate thermalization hypothesis,” *Phys. Rev. Lett.* **119**, 201 (2017).
- ⁷² Naoto Shiraishi, “Connection between quantum-many-body scars and the Affleck–Kennedy–Lieb–Tasaki model from the viewpoint of embedded Hamiltonians,” *Journal of Statistical Mechanics: Theory and Experiment* **2019**, 083103 (2019).
- ⁷³ Fernando GSL Brandao, Matthias Christandl, Aram W Harrow, and Michael Walter, “The mathematics of entanglement,” *arXiv preprint arXiv:1604.01790* (2016).
- ⁷⁴ Bruno Sciola and Giulio Biroli, “Dynamical transitions and quantum quenches in mean-field models,” *Journal of Statistical Mechanics: Theory and Experiment* **2011**, P11003 (2011).
- ⁷⁵ Takashi Mori, “Classical ergodicity and quantum eigenstate thermalization: Analysis in fully connected Ising ferromagnets,” *Phys. Rev. E* **96**, 012134 (2017).
- ⁷⁶ “Supplemental online material,”.
- ⁷⁷ Ole Christensen *et al.*, *An introduction to frames and Riesz bases* (Springer, 2016).
- ⁷⁸ A. G. Green, C. A. Hooley, J. Keeling, and S. H. Simon, “Feynman path integrals over entangled states,” (2016), [arXiv:1607.01778 \[cond-mat.str-el\]](https://arxiv.org/abs/1607.01778).
- ⁷⁹ Lucas Hackl, Tommaso Guaita, Tao Shi, Jutho Haegeman, Eugene Demler, and Ignacio Cirac, “Geometry of variational methods: dynamics of closed quantum systems,” (2020), [arXiv:2004.01015 \[quant-ph\]](https://arxiv.org/abs/2004.01015).
- ⁸⁰ Jean-Pierre Gazeau, *Coherent States in Quantum Physics* (Wiley-VCH, 2009).
- ⁸¹ Milton Abramowitz and Irene A Stegun, *Handbook of mathematical functions with formulas, graphs, and mathematical tables*, Vol. 55 (US Government printing office, 1948).
- ⁸² Ingemar Bengtsson and Karol Życzkowski, *Geometry of Quantum States* (Cambridge, 2006).
- ⁸³ Martin C Gutzwiller, *Chaos in classical and quantum mechanics*, Vol. 1 (Springer Science & Business Media, 2013).
- ⁸⁴ Cheng-Ju Lin, Vladimir Calvera, and Timothy H Hsieh, “Quantum many-body scar states in two-dimensional Rydberg atom arrays,” (2020), [arXiv:2003.04516 \[cond-mat.quant-gas\]](https://arxiv.org/abs/2003.04516).
- ⁸⁵ AA Michailidis, CJ Turner, Z Papić, DA Abanin, and M Serbyn, “Stabilizing two-dimensional quantum scars by deformation and synchronization,” (2020), [arXiv:2003.02825 \[quant-ph\]](https://arxiv.org/abs/2003.02825).
- ⁸⁶ Roderich Moessner and Kumar S Raman, “Quantum dimer models,” in *Introduction to Frustrated Magnetism* (Springer, 2011) pp. 437–479.

- ⁸⁷ Daniel S. Rokhsar and Steven A. Kivelson, “Superconductivity and the quantum hard-core dimer gas,” *Phys. Rev. Lett.* **61**, 2376–2379 (1988).
- ⁸⁸ Paul H Algoet and Thomas M Cover, “A Sandwich Proof of the Shannon-McMillan-Breiman Theorem,” *The Annals of Probability* **16**, 899–909 (1988).
- ⁸⁹ Richard V Kadison and John R Ringrose, *Fundamentals of the Theory of Operator Algebras*, Elementary Theory, Vol. 1 (Academic Press, 1983).

Supplemental Online Material for “Correspondence principle for many-body scars in ultracold Rydberg atoms”

C. J. Turner, J.-Y. Desautels, K. Bull and Z. Papić

School of Physics and Astronomy, University of Leeds, Leeds LS2 9JT, United Kingdom

In this supplementary material, we present analytical derivations of class sizes and operator matrix elements projected to the symmetric subspace \mathcal{K} . We elucidate in detail the connection between \mathcal{K} and the TDVP subspace \mathcal{M} , proving that $\mathcal{K} = \text{span}\mathcal{M}$. We discuss the quality of revivals and state transfer in large systems within the symmetric subspace approximation. Finally, we provide details on the path-integral quantisation in the constrained space.

SI. Analytical derivation of class sizes and matrix elements

A. Class sizes

In the symmetric subspace, each basis state is a symmetric superposition of product states in the full (constrained) Hilbert space. All these states have the same number of excitations on each sublattice, and so they belong to the equivalence class $(n_1, n_2)_N$. The basis states of the subspace are then defined as

$$|(n_1, n_2)_N\rangle = \frac{1}{\sqrt{\#(n_1, n_2)_N}} \sum_{\phi \in (n_1, n_2)} |\phi\rangle, \quad (\text{S1})$$

where $\#(n_1, n_2)_N$ is the size of the corresponding class. In order to compute the matrix elements of H , we now derive an analytical expression for the class size using a recurrence relation for periodic boundary conditions.

We start with the simple case where $n_1 = 0$, meaning that there are no excitations on the first sublattice. Then the Rydberg constraints are irrelevant and the class size corresponds to the number of ways to place n_2 identical excitations in $N/2$ sites. This leads to

$$\#(0, n_2)_N = \frac{(N/2)!}{n_2!(N/2 - n_2)!} = \binom{N/2}{n_2}, \quad (\text{S2})$$

which is simply a binomial coefficient.

For $n_1 \neq 0$, we want to obtain a relation between $\#(n_1, n_2)_N$ and $\#(n_1 - 1, n_2)_{N-2}$. This can be done by counting the number of product states in the class starting with the pattern $|\bullet\circ\dots\rangle$ in two different ways. This quantity is denoted by $D_{\bullet\circ}(N, n_1, n_2)$, and can be computed using the operator $S_{\bullet\circ}^i$, which is a projector on all states having $\bullet\circ$ on sites i and $i + 1$. So for any product state $|\psi\rangle$ in the full Hilbert space,

$$S_{\bullet\circ}^i |\psi\rangle = \begin{cases} |\psi\rangle & \text{if } |\psi\rangle = |\underbrace{\dots}_{i-1} \bullet \circ \underbrace{\dots}_{N-i-2}\rangle \\ 0 & \text{otherwise.} \end{cases} \quad (\text{S3})$$

This allows us to compute

$$D_{\bullet\circ}(N, n_1, n_2) = \sum_{\substack{|\psi\rangle \in \\ (n_1, n_2)_N}} \langle \psi | S_{\bullet\circ}^1 | \psi \rangle = \frac{2}{N} \sum_{j=0}^{N/2-1} \sum_{\substack{|\psi\rangle \in \\ (n_1, n_2)_N}} \langle \psi | S_{\bullet\circ}^{2j+1} | \psi \rangle = \frac{2n_1}{N} \#(n_1, n_2)_N. \quad (\text{S4})$$

Here we used the fact that the sum over the class elements is invariant under translation of 2 sites. The two sums can then be swapped and the sum over j simply counts the number of excitations on the first sublattice, and thus will give n_1 for every state in this class.

The second way of counting $D_{\bullet\circ}(N, n_1, n_2)$ relies on separating the first two sites from the rest of the chain. Any state $|\psi\rangle \in (n_1, n_2)_N$ with the pattern $|\bullet\circ\dots\rangle$ can be rewritten as $|\bullet\circ\rangle \otimes |\phi\rangle$, where $|\phi\rangle \in (n_1 - 1, n_2)_{N-2}$ with its last site not excited. The fraction of states in $(n_1 - 1, n_2)_{N-2}$ satisfying this condition is given by $1 - \frac{n_2}{N/2-1} = \frac{N/2-1-n_2}{N/2-1}$. Accounting for the size of this class leads to

$$D_{\bullet\circ}(N, n_1, n_2) = \frac{N/2 - 1 - n_2}{N/2 - 1} \#(n_1 - 1, n_2)_{N-2}. \quad (\text{S5})$$

Putting together equations Eq. (S4) and Eq. (S5) gives the recurrence relation

$$\#(n_1, n_2)_N = \frac{N}{2n_1} \frac{N/2-1-n_2}{N/2-1} \#(n_1-1, n_2)_{N-2}. \quad (\text{S6})$$

Using Eq. (S2) as the initial condition, it is straightforward to use this recurrence to obtain the general class size

$$\#(n_1, n_2)_N = \frac{\frac{N}{2} \binom{\frac{N}{2} - n_1 - n_2}{n_2}}{\left(\frac{N}{2} - n_1\right) \left(\frac{N}{2} - n_2\right)} \binom{\frac{N}{2} - n_1}{n_2} \binom{\frac{N}{2} - n_2}{n_1}. \quad (\text{S7})$$

B. Matrix elements

As the PXP Hamiltonian removes or adds a single excitation, $|n_1, n_2\rangle$ only has non-zero matrix elements with $|n_1 \pm 1, n_2\rangle$ and $|n_1, n_2 \pm 1\rangle$. Using the Hermiticity of H and the exchange symmetry $n_1 \rightleftharpoons n_2$, only one of these

Applying H_1^+ to any state in (n_1, n_2, m_1, m_2) gives m_1 distinct states, one for each excitable site. This allows one to compute the matrix element

$$\left(H\right)_{(n_1, n_2)}^{(n_1+1, n_2)} = \frac{\sum_{m_1, m_2} m_1 \#(n_1, n_2, m_1, m_2)}{\sqrt{\#(n_1, n_2) \#(n_1+1, n_2)}}. \quad (\text{S18})$$

Because of the Hermiticity of H , Eq. (S9) can be used to derive the identity

$$\sum_{m_1, m_2} m_1 \#(n_1, n_2, m_1, m_2) = (n_1+1) \#(n_1+1, n_2). \quad (\text{S19})$$

Using these new classes and identities, it is now possible to compute the matrix element for $\hat{K}(H_1^+ H_1^-)$ acting on $|(n_1, n_2)\rangle$. First, the number of states in the class needs to be expressed as $\#(n_1, n_2) = \sum_{m_1, m_2} \#(n_1, n_2, m_1, m_2)$. Acting with H_1^- simply gives a factor of n_1 for all states, leaving us with $n_1 \sum_{m_1, m_2} \#(n_1, n_2, m_1, m_2)$ elements. It also creates an additional excitable site, which means that acting with H_1^+ leads to

$$\begin{aligned} n_1 \sum_{m_1, m_2} (m_1 + 1) \#(n_1, n_2, m_1, m_2) \\ = n_1 (n_1 + 1) \#(n_1 + 1, n_2) + n_1 \#(n_1, n_2) \end{aligned} \quad (\text{S20})$$

contributions, where identities Eq. (S17) and Eq. (S19) were used to resolve the sum. With the normalisation this amounts to

$$\begin{aligned} A_{1,1}^{+,-}(n_1, n_2) &= n_1 (n_1 + 1) \frac{\#(n_1 + 1, n_2)}{\#(n_1, n_2)} + n_1 \\ &= n_1 \frac{(\frac{N}{2} - n_1 - n_2 - 1)(\frac{N}{2} - n_1 - n_2)}{\frac{N}{2} - n_1 - 1} + n_1. \end{aligned} \quad (\text{S21})$$

The equivalent quantity for $(\hat{K}(H))^2$ is

$$\begin{aligned} B_{1,1}^{+,-}(n_1, n_2) &= n_1^2 \frac{\#(n_1, n_2)}{\#(n_1 - 1, n_2)} \\ &= n_1 \frac{(\frac{N}{2} - n_1 - n_2)(\frac{N}{2} - n_1 - n_2 + 1)}{\frac{N}{2} - n_1}. \end{aligned} \quad (\text{S22})$$

B. Off-diagonal elements : $H_1^+ H_2^-$

This case is trickier because it involves the mixing of m_1 and m_2 . To simplify the computation, it is better to focus on the unnormalised matrix element $\bar{A}_{1,2}^{+,-}(n_1, n_2 + 1)$ such that

$$\bar{A}_{1,2}^{+,-}(n_1, n_2 + 1) = \mathcal{N} \langle (n_1 + 1, n_2) | H_1^+ H_2^- | (n_1, n_2 + 1) \rangle, \quad (\text{S23})$$

where $\mathcal{N} = \sqrt{\#(n_1 + 1, n_2) \#(n_1, n_2 + 1)}$. The rightmost state is $|(n_1, n_2 + 1)\rangle$ because the focus of the computation is on the intermediate state $|(n_1, n_2)\rangle$. When acting with

H_2^- on $|(n_1, n_2 + 1)\rangle$, each state in (n_1, n_2, m_1, m_2) gains a factor of m_2 because of the number of states contributing. The same is true for the left half, acting with H_1^- on $|(n_1 + 1, n_2)\rangle$, gives a factor of m_1 . Inserting the identity in the middle as $\frac{|(n_1, n_2)\rangle \langle (n_1, n_2)|}{\#(n_1, n_2)}$ gives

$$\begin{aligned} \bar{A}_{1,2}^{+,-}(n_1, n_2 + 1) &= \sum_{m_1, m_2} \frac{m_1 m_2 \#(n_1, n_2, m_1, m_2)}{\#(n_1, n_2)} \\ &= \frac{\sum_{m_1, m_2} m_1 m_2 \#(n_1, n_2, m_1, m_2)}{\sum_{m_1, m_2} \#(n_1, n_2, m_1, m_2)}. \end{aligned} \quad (\text{S24})$$

m_1 and m_2 can be viewed as random variables with a probability distribution proportional to $\#(n_1, n_2, m_1, m_2)$, then Eq. (S24) is simply the expectation value $E[m_1 m_2]$. The equivalent element for $(\hat{K}(H))^2$ can itself be understood as a product of the expectation values

$$\begin{aligned} E[m_1] E[m_2] &= \frac{(n_1 + 1) \#(n_1 + 1, n_2)}{\#(n_1, n_2)} \frac{(n_2 + 1) \#(n_1, n_2 + 1)}{\#(n_1, n_2)} \\ &= \frac{(\frac{N}{2} - n_1 - n_2 - 1)^2 (\frac{N}{2} - n_1 - n_2)^2}{(\frac{N}{2} - n_1 - 1)(\frac{N}{2} - n_2 - 1)}, \end{aligned} \quad (\text{S25})$$

where the relation between $E[m_i]$ and the matrix elements of $\hat{K}(H)$ is derived from Eqs. (S18–S19).

The subspace energy variance for $H_1^+ H_2^-$ is then given by the difference between equations Eq. (S24) and Eq. (S25), which is equal to the covariance of m_1 and m_2

$$\text{Cov}[m_1, m_2] = E[m_1 m_2] - E[m_1] E[m_2]. \quad (\text{S26})$$

Up to a multiplicative factor, this quantity is equal to

$$\begin{aligned} \sum_{m_1, m_2} \left\{ m_1 m_2 \left(\frac{N}{2} - n_1 - 1 \right) \left(\frac{N}{2} - n_2 - 1 \right) - \right. \\ \left. \left(\frac{N}{2} - n_1 - n_2 \right) \left(\frac{N}{2} - n_1 - n_2 - 1 \right) \right\} \times \#(n_1, n_2, m_1, m_2)_N. \end{aligned} \quad (\text{S27})$$

We will now make the assumption that $\frac{N}{2} - n_1 - 1 \neq 0$ and $\frac{N}{2} - n_2 - 1 \neq 0$ and demonstrate that this expression is identically zero. The cases $n_i = \frac{N}{2} - 1$ will be handled separately later.

For the purposes of this proof we will introduce an ordinary generating function for the elaborated class sizes,

$$[z^{N/2} x_1^{n_1} x_2^{n_2} y_1^{m_1} y_2^{m_2}] G = \#(n_1, n_2, m_1, m_2)_N. \quad (\text{S28})$$

From Eq. (S27) we can derive a differential equation for this generating function,

$$\begin{aligned} \left(\partial_{y_1} \partial_{y_2} (w \partial_w + x_1 \partial_{x_1} - 1) (w \partial_w + x_2 \partial_{x_2} - 1) \right. \\ \left. + (w \partial_w)^2 (w \partial_w - 1)^2 \right) G \Big|_{\substack{y_1=1 \\ y_2=1}} = 0 \end{aligned} \quad (\text{S29})$$

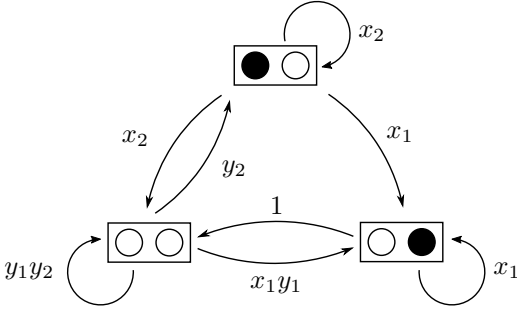


Figure S1. Finite state automaton diagram for the elaborated generating function. From this diagram we can read off the matrix elements of Eq. (S30).

where we have eliminated z by a change of variable in favour of $w = z/(x_1x_2)$. This equation is satisfied if and only if Eq. (S27) is equal to 0.

We will now derive a rational expression for G . Take a look at Fig. S1. Each state of this automaton is the state of the two sites on the (left) boundary of a partial configuration. Each arrow is an allowed gluing process. It takes the motif on the target of the arrow and glues it onto the left on the partial configuration producing a configuration with two more sites. The label on the arrows is a monomial factor which is picked up when following that gluing process. The x_1 and x_2 indeterminates mark when an excitation is added to the respective sublattices, whereas y_1 and y_2 are placed when we realise that we could have placed an excitation. The sum of all the execution paths of this automaton generates all the allowed configuration and marks them with the appropriate powers of the indeterminates. A process matrix for this automaton is the following,

$$M = \begin{pmatrix} y_1y_2 & y_2 & 1 \\ x_2 & x_2 & 0 \\ x_1y_1 & x_1 & x_1 \end{pmatrix}, \quad (\text{S30})$$

with which we can express the generating function as a Neumann series. The series clearly is convergent in some neighbourhood of $z = x_1 = x_2 = 0$ and $y_1 = y_2 = 1$ and so we may express it as

$$\begin{aligned} G(x_1, x_2, y_1, y_2; z) &= \sum_{N/2} z^{N/2} \text{Tr}\{M^{N/2}\} \\ &= \text{Tr}\{(\mathbb{1} - zM)^{-1}\} = \frac{3 - 2f_1z - f_2z^2}{1 - f_1z - f_2z^2 - f_3z^3}, \end{aligned} \quad (\text{S31})$$

where

$$f_1 = y_1y_2 + x_1 + x_2 \quad (\text{S32})$$

$$f_2 = x_1y_1(1-y_2) + x_2y_2(1-y_1) \quad (\text{S33})$$

$$f_3 = (1-y_1)(1-y_2). \quad (\text{S34})$$

This differs by an additive constant from the definition given previously, but this detail is unimportant. It is a lengthy albeit straightforward calculation to verify that

this indeed satisfies the differential equation Eq. (S29) as required.

Now we return to the deferred cases of when either $\frac{N}{2} - n_1 - 1 = 0$ or $\frac{N}{2} - n_2 - 1 = 0$. The first term $E[m_1m_2]$ vanishes because in either of these cases, for one of the sublattices, it is not possible to insert an excitation, hence $m_1m_2 = 0$. For the second term $E[m_1]E[m_2]$ the same reasoning implies that one of $\#(n_1 + 1, n_2)$ and $\#(n_1, n_2 + 1)$ must vanish. Thus the proposition is shown inclusive of the previously excluded cases.

C. Total subspace energy variance

The only non-zero matrix elements of the subspace energy variance are the diagonal ones given by Eqs. (S21–S22). Taking their difference leads to

$$\sigma_H^2 = \frac{n_1n_2(n_2 - 1)}{\left(\frac{N}{2} - n_1 - 1\right)\left(\frac{N}{2} - n_1\right)} + (1 \leftrightarrow 2) \quad (\text{S35})$$

for $|(n_1, n_2)\rangle$. The total subspace variance can also be obtained by tracing over all basis states

$$\text{Tr}[\sigma_H^2] = \frac{1}{9}\left(\frac{N}{2} - 3\right)\left(\frac{N}{2} - 2\right)\left(\frac{N}{2} - 1\right). \quad (\text{S36})$$

III. Proof that $\mathcal{M} \subseteq \mathcal{K}$

We will work in the general setting where there is a collection of N sites, an assignment of them onto d subsets and a projection operation which is diagonal in the computational basis. The state space \mathcal{M} are the projected 2-level coherent states and the vector space \mathcal{K} is the span of the symmetric combinations of the computational basis states with fixed occupation on each of the subsets. This setting subsumes the cases of the coherent-state TDVP ansatz for the PXP model from Ref. 9 developed further in Ref. 11, and also the generalisations on \mathbb{Z}_d initial states and tree-tensor networks.²⁴ The states in \mathcal{M} can be expressed using matrix product states with bond dimension $D = 2$. Similar to Ref. 11, we use the parametrisation

$$A^\bullet(\theta_j, \phi_j) = \begin{pmatrix} 0 & -ie^{i\phi_j}\sin(\frac{\theta_j}{2}) \\ 0 & 0 \end{pmatrix}, \quad A^\circ(\theta_j, \phi_j) = \begin{pmatrix} \cos(\frac{\theta_j}{2}) & 0 \\ \cos(\frac{\theta_j}{2}) & 0 \end{pmatrix}, \quad (\text{S37})$$

where A^\bullet is for an excited site and A° for an unexcited site. The chain is split into d sublattices, each with two parameters θ_j and ϕ_j . This produces N/d identical unit cells, and the corresponding (unnormalised) quantum state is

$$\sum_{\{\sigma\}} \text{Tr}[A^{\sigma_1}(\theta_1, \phi_1)A^{\sigma_2}(\theta_2, \phi_2)\dots A^{\sigma_d}(\theta_d, \phi_d) \cdot A^{\sigma_{d+1}}(\theta_1, \phi_1)\dots A^{\sigma_N}(\theta_d, \phi_d)] |\sigma_1, \dots, \sigma_N\rangle, \quad (\text{S38})$$

where the trace enforces periodic boundary conditions. This is equivalent to fixing sites $j, j+d, j+2d, \dots$ to $\cos\left(\frac{\theta_j}{2}\right)|\circ\rangle - ie^{i\phi_j}\sin\left(\frac{\theta_j}{2}\right)|\bullet\rangle$, with the additional application of a projector that annihilates configurations with neighbouring excitations.

Up to this point, only the symmetric subspace with two sublattices ($d=2$) has been considered. However, it is easy to see how to extend our previous results to d sublattices. The basis states $|(n_1, \dots, n_d)_N\rangle$ are then symmetric superpositions of product states with n_i excitations on the i -th sublattice. As in Sec. SI, recurrence relations for the class sizes can be found using combinatorics arguments. Once these are known, the matrix elements can be computed from them as it was done for $d=2$. We will now demonstrate that, for any value of d , all states in \mathcal{M} lie in the corresponding \mathcal{K} subspace.

In Eq. (S38), for each configuration of σ 's there is a product of N matrices of size 2×2 . For the moment, suppose that there is at least one excitation in the configuration. Then this sequence can be segmented into blocks with the following pattern: the leftmost matrix corresponds to an excitation and all the others are vacancies. Because of the cyclic property of the trace, we can also assume that the leftmost matrix in Eq. (S38) corresponds to an excitation and rewrite the quantity inside the trace as

$$\prod_{\text{Blocks}} \left[A^\bullet(\theta_j, \phi_j) \prod_{l=1}^m A^\circ(\theta_{j+l}, \phi_{j+l}) \right], \quad (\text{S39})$$

where the indices of the angles are periodic in d , meaning that $\theta_{d+j} = \theta_j$. From Eq. (S37), it is easy to compute the product of two vacancy matrices

$$A^\circ(\theta_k, \phi_k) A^\circ(\theta_j, \phi_j) = \cos\left(\frac{\theta_j}{2}\right) \begin{pmatrix} \cos\left(\frac{\theta_k}{2}\right) & 0 \\ \cos\left(\frac{\theta_k}{2}\right) & 0 \end{pmatrix}. \quad (\text{S40})$$

Therefore, in each block the whole trail of vacancy matrices on the right can be reduced to a single vacancy matrix and a product of cosines. The product between an excitation matrix and a vacancy matrix can also be simplified as

$$A^\bullet(\theta_k, \phi_k) A^\circ(\theta_j, \phi_j) = -ie^{i\phi_k} \sin\left(\frac{\theta_k}{2}\right) \cos\left(\frac{\theta_j}{2}\right) B, \quad (\text{S41})$$

where $B := \begin{pmatrix} 1 & 0 \\ 0 & 0 \end{pmatrix}$. Finally, it is easy to see from Eq. (S37) that the product of two excitation matrices gives 0. So this parametrisation guarantees that each block has at least one vacancy matrix on the right, and that Eq. (S39) can be written as

$$\prod_{\text{Blocks}} \left[-B ie^{i\phi_j} \sin\left(\frac{\theta_j}{2}\right) \prod_{l=1}^m \cos\left(\frac{\theta_{j+l}}{2}\right) \right]. \quad (\text{S42})$$

This is a product of collinear (and hence commuting) matrices, and the effect of the trace on it is trivial. The last step is to count the number of blocks with a leftmost matrix with index j . For any configuration, it is simply given by the number of excitations in the corresponding sublattice. This means that each excitation in the sublattice j gives a factor of $ie^{i\phi_j} \sin(\theta_j/2)$. The other sites in this sublattice are free and give a factor of $\cos(\theta_j/2)$ each. This means that each configuration n_1, \dots, n_k has a prefactor of

$$\prod_{j=1}^d c_{\bullet,j}^{n_j} c_{\circ,j}^{N/d-n_j} \quad \text{with} \quad \begin{cases} c_{\bullet,j} = -ie^{i\phi_j} \sin\left(\frac{\theta_j}{2}\right), \\ c_{\circ,j} = \cos\left(\frac{\theta_j}{2}\right). \end{cases} \quad (\text{S43})$$

As this term only depends on the sublattice on which the excitations are placed and not on the actual sites, it can be exactly expressed in the symmetric subspace. Inserting this result into Eq. (S38) and accounting for the number of such configurations in the product basis means that in the symmetric subspace the state $|\{\theta_i, \phi_i\}_N\rangle$ can be rewritten as

$$\sum_{n_1, \dots, n_d} \sqrt{\#(n_1, \dots, n_d)} \left(\prod_{j=1}^d c_{\bullet,j}^{n_j} c_{\circ,j}^{N/d-n_j} \right) |(n_1, \dots, n_d)_N\rangle. \quad (\text{S44})$$

Returning to the excluded case where there are no excitations, it is easy to see from Eq. (S40) that it will give

$$\prod_{i=j}^d \left[\cos\left(\frac{\theta_j}{2}\right) \right]^{N/d} = \prod_{j=1}^d c_{\circ,j}^{N/d}. \quad (\text{S45})$$

As $\sqrt{\#(0, \dots, 0)} = 1$, it satisfies Eq. (S44). This completes the proof that $\mathcal{M} \subseteq \mathcal{K}$, as Eq. (S44) expresses every point of \mathcal{M} as a linear combination of vectors in \mathcal{K} .

SIV. Proof that $\mathcal{K} = \text{span } \mathcal{M}$

Section SIII establishes that $\mathcal{M} \subseteq \mathcal{K}$. We now claim that the relation between these two spaces is stronger, and that $\mathcal{K} = \text{span } \mathcal{M}$. For simplicity, in this section we will work with the complex parametrisation of \mathcal{M} ,

$$|\psi_N(z)\rangle = \sum_{n_1, \dots, n_d} \sqrt{\#(n_1, \dots, n_d)_N} \prod_{a=1}^d z_a^{n_a} |(n_1, \dots, n_d)_N\rangle. \quad (\text{S46})$$

This parametrisation, like the coherent-state parametrisation of section SIII, may fail to be injective. This happens for the PXP model when $\theta_a = \pm\pi/2$ for some a . This is a defect with the space \mathcal{M} , where \mathcal{M} fails to be locally Euclidean, rather than with the parametrisations.

We will now be considering two ordered bases B and B' where $\text{span } B = \mathcal{K}$ and $\text{span } B' \subseteq \text{span } \mathcal{M}$. The first basis B is defined as

$$B_{n_1, \dots, n_d} = \sqrt{\#(n_1, \dots, n_d)_N} |(n_1, \dots, n_d)_N\rangle, \quad (\text{S47})$$

where the multi-index n_1, \dots, n_d is taken to include values such as $N/2, \dots, N/2$ for which the basis vector is a zero-vector. This makes B an over-complete and linearly dependent basis for \mathcal{K} ; this is done to provide the multi-index with a natural Cartesian product structure.

In order to define the second basis B' we will first need to choose a set of distinct coordinate values $z_{a,(1)}, \dots, z_{a,(N/2+1)}$, for each dimension $a = 1, \dots, d$. We define the basis B' using the complex parametrisation as

$$B'_{i_1, \dots, i_d} = |\psi(z_{1,(i_1)}, \dots, z_{d,(i_d)})\rangle. \quad (\text{S48})$$

We can interpret this basis as coordinate-aligned grid of points, where we have sampled the \mathcal{M} -valued polynomial $|\psi(z_1, \dots, z_d)\rangle$ to provide our basis vectors.

Disregarding possible linear dependence in B and B' , our goal of showing that $\text{span } B' = \text{span } B$ is equivalent to how the coefficients of a polynomial may be determined by evaluating at a sufficient number of distinct points. This motivates introducing for each $a = 1, \dots, d$ a Vandermonde matrix

$$Q_a = \begin{pmatrix} 1 & z_{a,(1)} & z_{a,(1)}^2 & \cdots & z_{a,(1)}^{|a|} \\ 1 & z_{a,(2)} & z_{a,(2)}^2 & \cdots & z_{a,(2)}^{|a|} \\ \vdots & \vdots & \vdots & \ddots & \vdots \\ 1 & z_{a,(|a|+1)} & z_{a,(|a|+1)}^2 & \cdots & z_{a,(|a|+1)}^{|a|} \end{pmatrix}, \quad (\text{S49})$$

where $|a|$ is the number of sites in sublattice $|a|$. Since the $z_{a,(1)}, \dots, z_{a,(N/2+1)}$ are all distinct each Q_a is invertible.

These matrices can be used to relate the two ordered bases using $Q = \bigotimes_{a=1}^d Q_a$ providing two equations,

$$B' = QB \quad \text{and} \quad B = Q^{-1}B'. \quad (\text{S50})$$

These can be read to mean that each basis vector in B' is a linear combination of those in B , and vice-versa, i.e. $\text{span } B = \text{span } B'$. Recalling that B is a complete basis for \mathcal{K} and that every vector in B' is contained in \mathcal{M} , we find the containment, $\text{span } \mathcal{M} \supseteq \text{span } B' = \text{span } B = \mathcal{K}$, which completes the proof.

SV. Bipartite entropy in the symmetric subspace

Computing the von Neumann bipartite entropy in the symmetric subspace is not straightforward due to the non-local definition of the basis states. Consider a spin chain of length N with periodic boundary conditions and cut it into two subsystems of size N_L and N_R , respectively. Let quantities related to the left part be denoted by the subscript L and the ones related to the right part by the subscript R . The simplest way to compute the bipartite entropy for this cut for a basis state $|(n_1, n_2)_N\rangle$ would be to express it in the full Hilbert space and proceed from there. However this is suboptimal as it would strongly limit our ability to study large systems. Instead, the structure of the subspace can be exploited in order to write the states in the right and left subsystems in their

respective symmetric subspaces. To simplify the computations, we only consider cases where the right and left subsystems are of even size. If nothing is specified, we consider the cut into two subsystems of equal size, meaning that the full system has size $N = 4M$, $M \in \mathbb{N}$, and the two subsystems have size $N_L = N_R = 2M$.

While the full system has periodic boundary conditions, the subsystems must have open boundary conditions. Consider the cut $|\bullet\bullet\bullet\bullet\bullet\bullet\rangle = |\bullet\bullet\bullet\rangle \otimes |\bullet\bullet\bullet\rangle$, it is clear that the left part violates the Rydberg constraint if periodic boundary conditions are assumed. Conversely, the two subsystems $|\bullet\bullet\bullet\rangle$ and $|\bullet\bullet\bullet\rangle$ respect the Rydberg constraints individually but their tensor product does not. This simple case shows that we must further subdivide the classes in the left and right subsystems based on the value of the extremal sites.

Let us denote by $(n_1, n_2, a, b)_N$, $a, b \in 0, 1$ the class of states in $(n_1, n_2)_N$ with the additional constraint that the leftmost site is defined by a and the rightmost site is by b . The convention used is that the leftmost site is unexcited if $a = 0$ and excited if $a = 1$, and the same hold for b and the rightmost site. Then $|(n_1, n_2, a, b)_N\rangle$ is the normalised symmetric superposition of all product states in $(n_1, n_2, a, b)_N$. Using these states, the relevant Schmidt decomposition for $|(n_1, n_2)_N\rangle$ is

$$\sum_{\substack{l_1, l_2 \\ r_1, r_2}} \sum_{\substack{a_L, b_L \\ a_R, b_R}} \alpha |(l_1, l_2, a_L, b_L)_{N_L}\rangle \otimes |(r_1, r_2, a_R, b_R)_{N_R}\rangle, \quad (\text{S51})$$

where the sums on l_i and r_i run from 0 to $\frac{N}{2}$, the sums on all a and b run from 0 to 1, and α depends on n_1, n_2 and on all the summation indices. This decomposition includes terms that are forbidden by Rydberg constraints such as $|(\frac{N_L}{2}, \frac{N_L}{2}, a_L, b_L)_{N_L}\rangle$. However we will see later that the coefficient α corresponding to these will naturally be zero.

To compute α , selection rules can be stated. The most obvious one is the conservation of the number of excitations on each sublattice, which tells us that $l_i + r_i = n_i$. More formally, it means that α needs to include a term

$$\beta_{l_1, l_2, r_1, r_2}^{n_1, n_2} = \delta_{l_1+r_1, n_1} \delta_{l_2+r_2, n_2}, \quad (\text{S52})$$

where $\delta_{i,j}$ is the Kronecker delta. The selection rule on the a and b is also simple: a_L and b_R cannot both be 1 and neither can b_L and a_R as this would correspond to neighbouring excitations. This can be expressed as

$$\eta_{a_L, b_L}^{a_R, b_R} = (1 - a_L b_R) (1 - b_L a_R). \quad (\text{S53})$$

The last step is to compute the contribution of each class $(n_1, n_2, a, b)_N$. Each product state in $(n_1, n_2)_N$ corresponds to a single state in $(l_1, l_2, a_L, b_L)_{N_L} \otimes (r_1, r_2, a_R, b_R)_{N_R}$. So the only multiplicative factors that enter the equation are the normalisation ones. For each combination of the l_i, r_i, a, b the contribution to α is simply given by

$$\frac{\sqrt{\#(l_1, l_2, a_L, b_L)_{N_L}} \sqrt{\#(r_1, r_2, a_R, b_R)_{N_R}}}{\sqrt{\#(n_1, n_2)_N}}. \quad (\text{S54})$$

These class sizes can be computed using the same arguments as in section SI, keeping in mind that the two subsystems have open boundary conditions. To separate the contributions of the left and right parts we define

$$\gamma_{n_1, n_2, a, b}^N = \sqrt{\#(n_1, n_2, a, b)_N}. \quad (\text{S55})$$

This coefficient ensures that all states in the Schmidt decomposition respect the Rydberg constraint. Indeed, if a state is incompatible with it, its class size must be 0 and so is the corresponding γ .

Using Eqs. (S52–S55), the coefficients α from Eq. (S51) can be written as

$$\alpha = \frac{\beta_{l_1, l_2, r_1, r_2}^{n_1, n_2} \eta_{a_L, b_L}^{a_R, b_R} \gamma_{l_1, l_2, a_L, b_L}^{N_L} \gamma_{r_1, r_2, a_R, b_R}^{N_R}}{\sqrt{\#(n_1, n_2)_N}}. \quad (\text{S56})$$

From this Schmidt decomposition it is straightforward to compute the entanglement spectrum and the von Neumann entropy.

SVI. Revivals in large- N limit

The main feature of the PXP model is the revivals of the wavefunction that can be seen for some initial product states. This effect is the strongest when starting from the Néel state $|\mathbb{Z}_2\rangle = |\bullet\circ\bullet\circ\dots\rangle$ or the anti-Néel state $|\bar{\mathbb{Z}}_2\rangle = |\circ\bullet\circ\bullet\dots\rangle$. When starting in one of these states, after a time T the wavefunction comes back to itself. Furthermore, when starting in the state $|\mathbb{Z}_2\rangle$, after a half-period the wavefunction will be $|\bar{\mathbb{Z}}_2\rangle$, and vice-versa. In the remainder of this section we will refer to this as state transfer. However, these revivals (and state transfers) are not perfect and decay with time. On the other hand, TDVP shows a periodic orbit going through both the Néel and anti-Néel states for an infinite system. In this section we study the finite-size dependence of revivals in the symmetric subspace.

To measure the quality of the revivals, the wavefunction fidelity and the entanglement entropy are used. Starting from the Néel state $|(\frac{N}{2}, 0)_N\rangle = |\mathbb{Z}_2\rangle$, the Schrödinger time evolution is generated by e^{-iHt} . The fidelity of revival is then

$$f_{Rev}(t) = \left| \langle (N/2, 0)_N | e^{-iHt} | (N/2, 0)_N \rangle \right|^2 \quad (\text{S57})$$

and the fidelity of state transfer is

$$f_{Trans}(t) = \left| \langle (0, N/2)_N | e^{-iHt} | (N/2, 0)_N \rangle \right|^2. \quad (\text{S58})$$

For the entanglement entropy we use the von Neumann bipartite entropy, as computed in Sec. SV. We also restrict our study to systems of size $N = 4M$, $M \in \mathbb{N}$, and we cut them into two equally sized subsystems. From this we define the entropy as

$$S(t) = S(e^{-iHt} |(N/2, 0)_N\rangle). \quad (\text{S59})$$

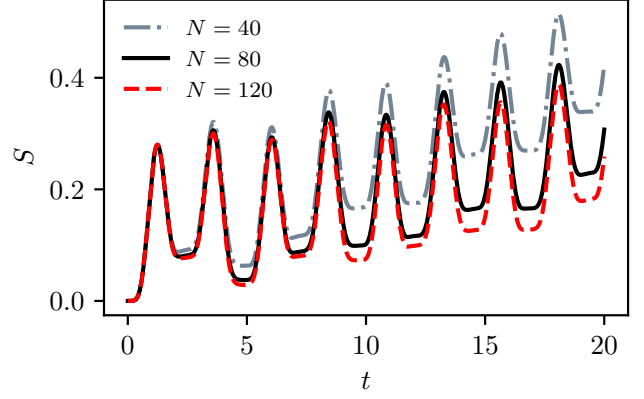


Figure S2. Bipartite von Neumann entropy of $e^{-iHt} |\mathbb{Z}_2\rangle$ in the symmetric subspace. As N increases, the entropy growth with time becomes slower.

As both the Néel and anti-Néel states are product states in the full Hilbert space, their entanglement entropy is 0. From the exact PXP model, we expect the first state transfer to happen around $t = 2.35$ and the first revival around $t = 4.70$.¹⁰ This can be seen in the entropy plot in Fig. S2. From this plot it is clear that the revivals get enhanced as N increases, but the quality of the first state transfer vary very little with system size. To obtain a more rigorous scaling, let us define the times of the first revival and state transfer, respectively, as

$$t_1 = \arg \max_{3 < t < 6} (f_{Rev}(t)), \quad (\text{S60})$$

$$t_{1/2} = \arg \max_{1 < t < 4} (f_{Trans}(t)). \quad (\text{S61})$$

This leads to their respective fidelity and entropy

$$f_1 = f_{Rev}(t_1) \quad (\text{S62})$$

$$f_{1/2} = f_{Trans}(t_{1/2}) \quad (\text{S63})$$

$$S_1 = S(t_1) \quad (\text{S64})$$

$$S_{1/2} = S(t_{1/2}) \quad (\text{S65})$$

The scaling of these quantities with N can be seen in Fig. S3. The results for f_1 are consistent with the symmetric subspace having perfect revivals in the thermodynamic limit. However, the state transfer fidelity $f_{1/2}$ is clearly not converging towards 1.

To understand this behaviour we need to look at the different symmetry sectors as well as the different bands of states. With periodic boundary conditions, the relevant symmetry of the PXP model is translation. Because of the periodicity of the Néel state, it is only composed of eigenstates with momentum $k = 0$ or $k = \pi$. The scarred states of the top band belong alternatively to these two sectors, with the condition that the ground state always has $k = 0$. In the symmetric subspace, the quasimodes show the same behaviour with respect to these sectors.

Because our method allows us to access larger systems, more can be said about the scarred eigenstates.

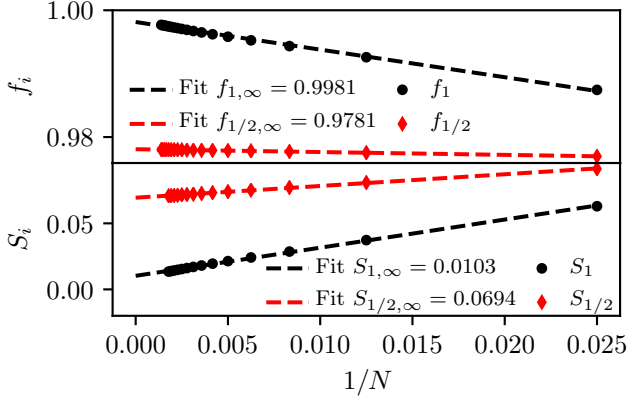


Figure S3. Wavefunction fidelity and bipartite entanglement entropy at the first state transfer ($f_{1/2}, S_{1/2}$) and revival (f_1, S_1). The fits shown are of the form $y = a \cdot 1/N + b$. The data is for sizes up to $N = 720$ for $f_{1/2}, f_1$ and for sizes up to $N = 560$ for $S_{1/2}, S_1$.

For example, scaling the system size shows that there is a constant fraction of them with an equal energy spacing around $E = 0$. As $N \rightarrow \infty$, the number of scarred quasimodes with a significant support on $|\mathbb{Z}_2\rangle$ scales as $\mathcal{O}(\sqrt{N})$. This means that, as we approach the thermodynamic limit, the only scarred eigenstates that have a non-zero overlap with the Néel state are evenly spaced.

Equal spacing of the energies with a difference ΔE implies perfect revivals with a period $T = 2\pi/\Delta E$. Without loss of generality, let us assume that the energy of the j -th eigenstate is equal to $j \cdot \Delta E$. After half a period, the phases of the even and odd eigenstates are

$$\phi_{2n} = \exp(-i\pi 2nE) = 1, \quad (\text{S66})$$

$$\phi_{2n+1} = \exp(-i\pi(2n+1)E) = -1. \quad (\text{S67})$$

Because of the alternation of momentum, only the $k = \pi$ states get a -1 factor as they are the odd ones. This exactly corresponds to the anti-Néel state as

$$\begin{aligned} |\bar{\mathbb{Z}}_2\rangle = \hat{T}|\mathbb{Z}_2\rangle &= \sum_{|E\rangle \in k=0} \alpha_E^0 \hat{T}|E\rangle + \sum_{|E\rangle \in k=\pi} \alpha_E^\pi \hat{T}|E\rangle \\ &= \sum_{|E\rangle \in k=0} \alpha_E^0 |E\rangle - \sum_{|E\rangle \in k=\pi} \alpha_E^\pi |E\rangle, \end{aligned} \quad (\text{S68})$$

where \hat{T} is the translation operator. This means that if only the top band were relevant there would be perfect revivals and perfect state transfer in \mathcal{K} .

However, the overlap between $|\mathbb{Z}_2\rangle$ and the non-scarred states is not negligible. In particular, we can explain the discrepancy between revivals and state transfers by looking at the second band. By "second band", we understand the band of states with the highest overlap with $|\mathbb{Z}_2\rangle$ after the scarred states (see figure S4). The quasimodes in this band have a much lower overlap with the Néel state than the scarred ones, but they also display the alternation between the two momentum sectors.

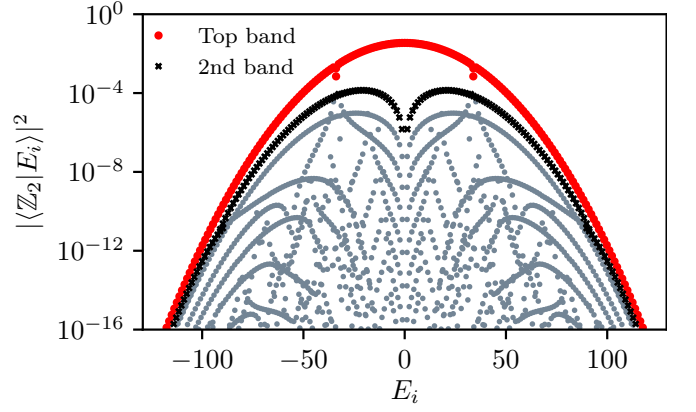


Figure S4. Overlap of the quasimodes with the Néel state for $N = 440$. The top-band (comprising the scarred eigenstates) is shown in red, and the second band in black.

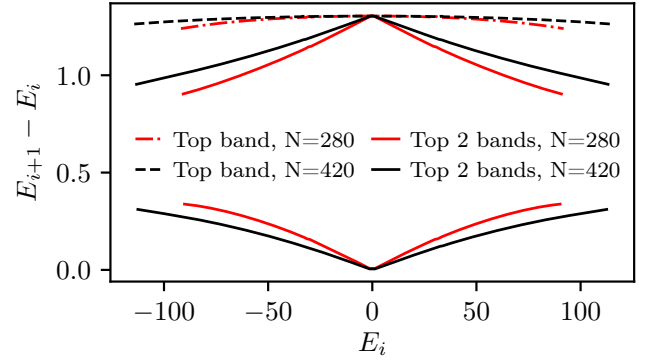


Figure S5. Energy difference between consecutive states in the top band and in the top two bands. Near $E = 0$, the two bands converge in energy, as can be seen from $E_{i+1} - E_i$ alternating between 0 and $\Delta E_{Top\ band}$.

Near $E = 0$, the two top bands converge towards the same energy values (Fig. S5), but with the opposite momentum value. Hence, in this region there are two eigenstates for each energy value, one with $k = 0$ and the other with $k = 1$. Because of that, the previous argument for state transfer does not hold anymore. However this has no effect on the energy spacing itself, so perfect revivals are still possible.

To summarise, in the symmetric subspace revivals get better as system size increases. While the finite size scaling is consistent with revival becoming perfect in the thermodynamic limit, it appears that the state transfer is never perfect because of the presence of the second band. This is to be contrasted with TDVP where both revivals and state transfers are exact.

SVII. Path-integral construction

If we seek to model a particular quantum dynamics with a classical analogue, we need a good understanding of the relationship between the two. In the main text we stated that in a certain situation we can view the TDVP classical system as the dequantisation of the original dynamics. This is in the sense of path-integral quantisation and with the proviso that from the state space we can form a good resolution of the identity. The following subsection will provide an asymptotic bound on the fluctuations in $S_\mu^{-1/2}$. This bound establishes convergence between the transformed and untransformed classical systems in the thermodynamic limit, and shows how a measure can be constructed with which the untransformed system quantises naturally.

A. Path integral dequantisation

The quantum path integral comes in a number of conventional representations: the position or momentum representations, corresponding to the Schrödinger formulation, and coherent-state representation, corresponding to the phase space formulation. In each case, the quantisation procedure involves an integral over all admissible paths, including those with non-stationary action, which assigns to each path a weight given by a measure function and a phase provided by the classical action. Because our starting point is instead a quantum system, we will instead take the backwards view where the path integral is defined by a classical limit. We are also provided with a collection of states $|x\rangle$ for which we assume that we can pick a measure μ to form a resolution of the identity,

$$\mathbb{1} = \int d\mu(x) |x\rangle \langle x|. \quad (\text{S69})$$

This allows us to represent the time evolution operator as an integral operator,

$$K_t(x', x) = \langle x' | e^{-iHt} | x \rangle, \quad (\text{S70})$$

which satisfies the homomorphism condition,

$$K_{a+b}(x'', x) = \int d\mu(x') K_a(x'', x') K_b(x', x). \quad (\text{S71})$$

In this way, the finite time propagator can be broken into a product of infinitesimal generators,

$$\begin{aligned} K_\epsilon(x_{n+1}, x_n) &= \langle x_{n+1} | x_n \rangle \left(1 - i\epsilon \frac{\langle x_{n+1} | H | x_n \rangle}{\langle x_{n+1} | x_n \rangle} + o(\epsilon^2) \right) \\ &= \exp \left(-i\epsilon \check{H} + \log T \right) + o(\epsilon^2), \end{aligned} \quad (\text{S72})$$

where

$$\check{H}(x_{n+1}, x_n) = \frac{\langle x_{n+1} | H | x_n \rangle}{\langle x_{n+1} | x_n \rangle} \quad (\text{S73})$$

and $T(x_{n+1}, x_n) = \langle x_{n+1} | x_n \rangle$. To deal with inner products across different times in a symmetric manner, half-steps can be introduced along the path,

$$\begin{aligned} T &= \left(\langle x_{n+\frac{1}{2}} | + \frac{\epsilon}{2} \langle \dot{x}_{n+\frac{1}{2}} | \right) \left(| x_{n+\frac{1}{2}} \rangle - \frac{\epsilon}{2} | \dot{x}_{n+\frac{1}{2}} \rangle \right) + o(\epsilon^2) \\ &= \langle x_{n+\frac{1}{2}} | x_{n+\frac{1}{2}} \rangle + \frac{\epsilon}{2} \left(\langle x_{n+\frac{1}{2}} | \dot{x}_{n+\frac{1}{2}} \rangle - \text{h.c.} \right) + o(\epsilon^2). \end{aligned}$$

The first term here gives another contribution to the path integral measure, and the second produces the kinetic term in the resulting Lagrangian,

$$\mathcal{L}(x, \dot{x}) = \frac{i}{2} \frac{\langle x | \dot{x} \rangle - \langle \dot{x} | x \rangle}{\langle x | x \rangle} - \check{H}. \quad (\text{S74})$$

Therefore, in this scenario where we can assume Eq. (S69), the TDVP action describes a valid classical limit and this path-integral provides a way to quantise it to recover the full quantum dynamics. Many of the familiar manifolds of quantum states, such as spin coherent states and matrix product states come with a natural choice for this measure which is the Haar measure for a transitive group action. The constrained coherent states of \mathcal{M} , however, are not of this type.

B. Fluctuation bounds for the frame operator

We begin by recalling the development of the transformed frame in the main text, before providing a proof for the asymptotic equivalence between the transformed and original frames. The first frame we considered involved the gauged parametrisation, Eq. (6), for \mathcal{M} equipped with the measure

$$d\mu = \left(\frac{N+1}{4\pi} \right)^2 \prod_{i=1,2} d\theta_i d\phi_i \sin \theta_i \cos^2 \frac{\theta_i}{2}. \quad (\text{S75})$$

This measure was motivated with an intuitive picture of fuzzy distinguishability on \mathcal{M} in the main text. From this the matrix elements of the frame operator S_μ in the symmetric basis can be expressed as an integral. The integral over the azimuthal parameters ϕ_a is oscillatory, ensuring that only the diagonal matrix elements are non-zero. The diagonal matrix elements are now computed,

$$\begin{aligned} (S_\mu)_{n_1, n_2} &= \#(n_1, n_2) \prod_{i=1}^2 \int_0^\pi d\theta_i \cos^{N-2n+3} \frac{\theta_i}{2} \sin^{2n_i+1} \frac{\theta_i}{2} \\ &= \#(n_1, n_2) \prod_{i=1}^2 \frac{\Gamma(n_i+1) \Gamma(\frac{N}{2}-n+2)}{\Gamma(\frac{N}{2}-n_i+3)}, \end{aligned} \quad (\text{S76})$$

where $n = n_1 + n_2$ and the integration is performed by taking a substitution $t_i = \cos^2(\theta_i/2)$ to place it in the form of an Euler integral. For periodic boundary conditions, we arrive at the rational function which was quoted in the main text,

$$(S_\mu)_{n_1, n_2} = \frac{\frac{N}{2}(\frac{N}{2}+1)^2(\frac{N}{2}-n)(\frac{N}{2}-n+1)^2}{(\frac{N}{2}-n_1)^{(3)}(\frac{N}{2}-n_2)^{(3)}}, \quad (\text{S77})$$

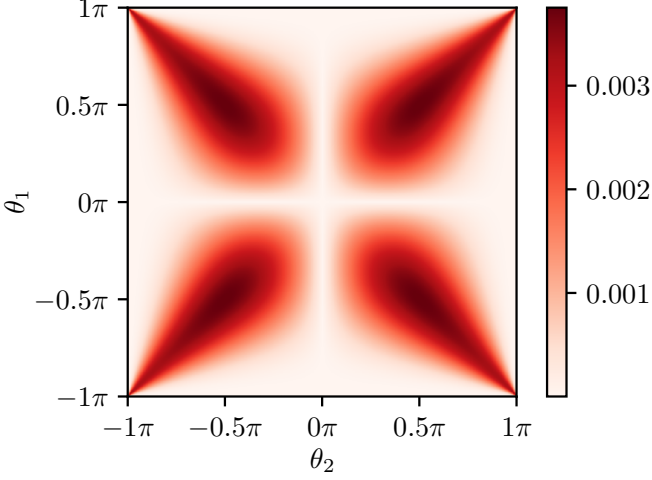


Figure S6. Transformed measure ν , Eq. (S80), in the thermodynamic limit, is non-negative and smooth away from the corner points.

where $(x)^{(n)}$ is the rising factorial or Pochhammer polynomial.⁸¹ This is best thought of as a function of the densities, n_a/N . Each linear factor in the numerator and denominator is a zero line or pole line, respectively, for the frame operator. For finite N and with the exception of the Néel states, these lines are outside of the domain of allowed densities. On the Néel states, the zero line $(N/2 - n)$ and pole line $(N/2 - n_a)$ intersect and cancel. In the vicinity of the Néel configurations, there are three ‘corner’ pole lines with fixed n_a and three ‘diagonal’ zero lines with fixed n , all within a distance of order $1/N$. As N increases the pole lines may become closer, but proportionally the zero lines also become closer. The scaling imparted by the zero lines to the residues of the approaching poles removes the divergence that would otherwise be caused by their approach. The additional cosine factors in the measure have the effect of adding two diagonal zero lines and one pole line passing-by each Néel state, and so without this there would be a residual pole at each Néel state, spoiling boundedness. Along the edge close to $(N - n) = 0$, there are no poles to cancel the zero lines so we can find matrix elements which are arbitrarily small as N increases. This provides a frame operator which is bounded and positive definite, even in the $N \rightarrow \infty$ limit, except along the triangle edge. This last point is not too concerning because we know that the dynamics avoids this part of \mathcal{K} , and is greatly preferable to leaving a simple pole on the most physically important states.

As emphasised in the main text, the frame operator found in this way is not suitable for quantisation. Its bounded and essentially positive-definite nature, however, leaves a measure which is qualitatively close to one in which a good resolution of the identity is found. Using the resulting frame operator we defined a transformed frame \mathcal{M} , which produces a resolution of the identity

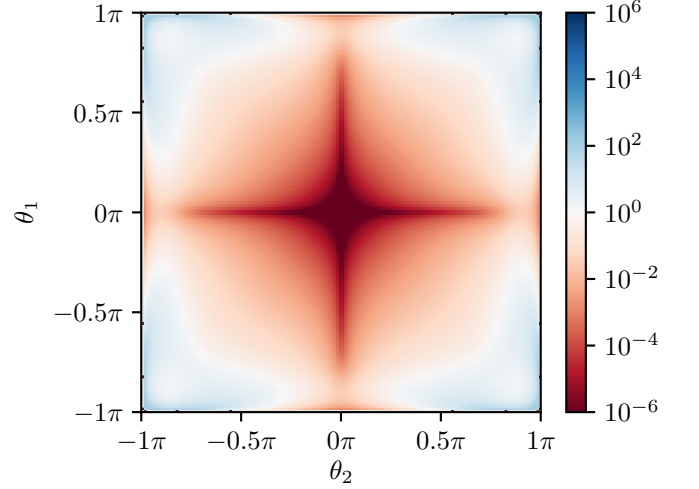


Figure S7. Variance in the $S_\mu^{-1/2}$ observable – see Eq. (S81) – divided by the expectation value, in the $\phi_a = 0$ section of the state space \mathcal{M} for $N = 128$. The fluctuations are strong only towards the corners in a region which shrinks as N increases.

from a congruence,

$$\mathbb{1}_{\mathcal{K}} = \int d\mu_{\theta, \phi} S_\mu^{-1/2} |\Psi(\theta, \phi)\rangle \langle \Psi(\theta, \phi)| S_\mu^{-1/2}. \quad (\text{S78})$$

This frame transformation potentially disturbs the states and obscures their physical meaning. We remedy this situation by approximating the effect of the frame transformation with a mere measure transformation,

$$\mathbb{1}_{\mathcal{K}} \approx S_\nu = \int d\nu_{\theta, \phi} |\Psi(\theta, \phi)\rangle \langle \Psi(\theta, \phi)|, \quad (\text{S79})$$

with the transformed measure,

$$d\nu = \left(\frac{\langle \Psi | S_\mu^{-1/2} | \Psi \rangle}{\langle \Psi | \Psi \rangle} \right)^2 d\mu, \quad (\text{S80})$$

which we claim is asymptotically exact. This measure in the thermodynamic limit is shown in Fig. S6, where it is seen to be smooth away from the corners. This allows the classical system produced by the retraction onto the gauged constrained coherent states to quantise naturally to the quantum dynamics projected into \mathcal{K} , as described in the previous subsection.

The error in the approximation can be characterised by the quantity,

$$\text{var}_\Psi[S_\mu^{-\frac{1}{2}}] = \frac{\langle \Psi | S_\mu^{-1} | \Psi \rangle}{\langle \Psi | \Psi \rangle} - \frac{\langle \Psi | S_\mu^{-1/2} | \Psi \rangle^2}{\langle \Psi | \Psi \rangle^2}. \quad (\text{S81})$$

This is the norm of the difference between the action of $S^{-1/2}$ on a state $|\Psi(\theta, \phi)\rangle$ and the action of multiplying by the state by the expectation value of that operator. It can be used to bound the difference between the measure-transformed frame operator S_ν and the identity,

and also the pointwise differences between untransformed and frame-transformed states.

In the remainder of this appendix we will show that $\text{var}_\Psi[S_\mu^{-1/2}] = O(1/N)$, which establishes the asymptotic equivalence between the frame transformation and a change of measure. The essential idea involves viewing each state $\Psi(\theta, \phi)$ as a stationary ergodic random process generating configurations. These correlations in $|\Psi\rangle$ are controlled by the correlation length ξ of connected correlation functions, which can be determined from the eigenvalues of the transfer matrix. This length-scale is finite almost everywhere on \mathcal{M} but diverges as the corner points are approached. Such a process satisfies the asymptotic equipartition property by the Shannon-McMillan-Breiman theorem.⁸⁸ Therefore, large deviations such as extensive fluctuations in n_1 and n_2 are suppressed exponentially and typical fluctuations are $O(1/\sqrt{N})$ in density. This suggests that the frame-transformation, which is diagonal in the density basis, would also become ‘diagonal’ in the frame \mathcal{M} and act as a scalar. In Fig. S7, we show how the variance behaves over \mathcal{M} for a fixed system size $N=128$. The fluctuations become strong only in the corners where ξ diverges.

We will use Eq. (S77) to view the operators S_μ^{-1} and $S_\mu^{-1/2}$ as functions of densities n_1/N and n_2/N which are then extended to the complex domain. We use f to refer to either of these functions in what follows. This function is shifted in the argument such that the density expectation value is at the origin and shifted in value with a constant term so that f vanishes there. In some places, it may be necessary to regularise the frame operator by introducing some $\epsilon > 0$ and replacing $S_\mu \mapsto S_\mu + \epsilon$ before the inverse, in order to displace any singularities into the complex domain. This is then removed at a later point by taking the $\epsilon \rightarrow 0$ limit after calculating some physical quantity insensitive to the singularity. For example, when applied to the frame operator for the transformed frame, this procedure yields a projector into the subspace of \mathcal{K} with the non-physical states removed.

Now, we model f as a Taylor series truncated at first order in each variable, and form a Cauchy bound to the remainder term. Pick a polydisc D centred around the mean densities with radii $0 < r_1 < \rho_1$ and $0 < r_2 < \rho_2$. We also choose some $0 < \beta < 1$, defining inner radii βr_1 and βr_2 . If possible, the radii should be chosen to include all subextensive density fluctuations for each finite N , but otherwise can be varied for an optimal bound in the final result. Since f is complex differentiable, its value interior to the disc can be related to that on the boundary by the multivariate Cauchy integral formula,

$$\begin{aligned} f(z_1, z_2) &= \oint_{\partial D} \frac{dw_1 dw_2}{(2\pi i)^2} \frac{f(w_1, w_2)}{(w_1 - z_1)(w_2 - z_2)} \\ &= f^{(1,0)} z_1 + f^{(0,1)} z_2 + f^{(1,1)} z_1 z_2 + R(z), \end{aligned} \quad (\text{S82})$$

where $R(z)$ is the remainder term and the other terms are the truncated Taylor series. The remainder term is found by expanding the geometric series and is bounded

by,

$$\begin{aligned} |R(z)| &\leq \left| \oint_{\partial D} \frac{f(w_1, w_2) dw_1 dw_2}{(w_1 - z_1)(w_2 - z_2)(2\pi i)^2} \left(\frac{z_1^2}{w_1^2} + \frac{z_2^2}{w_2^2} - \frac{z_1^2 z_2^2}{w_1^2 w_2^2} \right) \right| \\ &\leq \frac{M_{\partial D}}{r_1 r_2 (1 - \beta)^2} \left(\frac{|z_1|^2}{r_1^2} + \frac{|z_2|^2}{r_2^2} + \frac{|z_1 z_2|^2}{(r_1 r_2)^2} \right), \end{aligned} \quad (\text{S83})$$

where $M_{\partial D}$ appears as a uniform bound $|f(w_1, w_2)| \leq M_{\partial D}$ for all $(w_1, w_2) \in \partial D$. The constant factors in this bound are optimally independent of N (for sufficiently large N) because the smallest radii only admissible for larger N are bounded by at least $M_{\partial D} = O(r_1 + r_2)$.

Next, we relate these properties of S^{-1} and $S^{-1/2}$ as functions to their properties as operators. This is done with the Dunford-Riesz functional calculus,⁸⁹ which is a map $\Phi : \text{Hol}(D) \rightarrow \mathcal{L}(K)$ from holomorphic functions on a domain D to continuous linear operators on a Hilbert space K . It assigns to each function the Cauchy integral formula but with the geometric series replaced by resolvents of n_1 and n_2 , effectively promoting the indeterminants to operators. The result is a power series in the expectation values density fluctuation operators $\delta_i = (n_i - \langle n_i \rangle)/N$; equivalently, these are the central moments of the density observable distribution. In the spectral subspace outside the inner radii, the series may not converge, thereby failing to correspond to the original operator, and also the bound established does not apply. This region, however, corresponds to extensive fluctuations in the densities which are suppressed in probability exponentially with N due to the asymptotic equipartition property, wherever the correlation length is finite. The series divergence cannot overcome this, so we may safely use our Taylor series and bound on the remainder as if they were entire, whilst incurring only an error exponentially small in N . The first order terms vanish in expectation, hence the only remaining contributions provide a bound,

$$|\langle \Phi(f) \rangle| \leq |f^{(1,1)} \langle \delta_1 \delta_2 \rangle| + C \left[\frac{\langle \delta_1^2 \rangle}{r_1^2} + \frac{\langle \delta_2^2 \rangle}{r_2^2} + \frac{\langle \delta_1^2 \delta_2^2 \rangle}{r_1^2 r_2^2} \right], \quad (\text{S84})$$

where C is a constant factor from Eq. (S83). The moments appearing here are finite-order connected correlations functions which are all $O(1/N)$. This implies that the differences between the expectation value of e.g. S_μ^{-1} and its value as a function at the expected densities is only $O(1/N)$, and therefore so is the variance of $S_\mu^{-1/2}$.

Here we have shown that the frame operator fluctuations vanish as $O(1/\sqrt{N})$ for almost any point in \mathcal{M} in the thermodynamic limit. This is in agreement with what was found in Fig. 5 in the main text, where the Fubini-Study distance between untransformed and transformed state spaces was integrated for varying N . That calculation would also pick up a contribution due to the region of unphysical states with extensive correlation lengths which would decrease as the measure of this region decreases. Given the agreement with the $O(1/\sqrt{N})$ theory, it appears that the dominant contribution is instead the normal fluctuations discussed in this section.